

**MODELLING OF THREE-PHASE INDUCTION MACHINES FOR STUDYING
MOTOR-CONVERTER TRANSIENTS**

by

Sheraz Baig

B.Sc., Capital University of Science and Technology, Islamabad, 2019

A THESIS SUBMITTED IN PARTIAL FULFILLMENT OF
THE REQUIREMENTS FOR THE DEGREE OF

MASTER OF APPLIED SCIENCE

in

THE FACULTY OF GRADUATE AND POSTDOCTORAL STUDIES
(Electrical and Computer Engineering)

THE UNIVERSITY OF BRITISH COLUMBIA

(Vancouver)

August 2023

© Sheraz Baig, 2023

The following individuals certify that they have read, and recommend to the Faculty of Graduate and Postdoctoral Studies for acceptance, the thesis entitled:

Modelling of Three-Phase Induction Machines for Studying Motor-Converter Transients

submitted by Sheraz Baig in partial fulfillment of the requirements for

the degree of Master of Applied Science

in Electrical and Computer Engineering

Examining Committee:

Dr. Juri Jatskevich, Professor, Electrical and Computer Engineering, UBC

Supervisor

Dr. Hermann W. Dommel, Professor Emeritus, Electrical and Computer Engineering, UBC

Supervisory Committee Member

Dr. Yu Christine Chen, Associate Professor, Electrical and Computer Engineering, UBC

Supervisory Committee Member

Abstract

Variable frequency drives (VFDs) of low- and high-power levels are widely utilized in many commercial, industrial, vehicular, and propulsion applications, wherein typically, a squirrel-cage induction motor is fed from an inverter through a cable. To design and tune such systems, it is essential to develop efficient, accurate models of induction machines for studying the motor-converter interactions and low-to-high frequency phenomena. Depending on the required fidelity level, study objectives, and frequency range of interest, several classes of models of induction machines have been proposed in the literature, which can be generally classified into low-frequency and high-frequency models. Moreover, the motor-converter systems are typically the computational bottleneck in electromagnetic transient (EMT) simulators that are used in the power industry. It is desirable to have an induction machine model capable of capturing all transient phenomena in the range from dc to 10 MHz and can be effectively used for the analysis of VFD systems.

This thesis is focused on advancing the state-of-the-art induction machine and VFD modelling in state-variable-based (SVB) EMT programs. Specifically, this thesis presents an efficient modelling approach for system-level studies of VFDs, a reconfigurable star-delta CPVBR model for studying star-delta starting transients in motors, and a wideband decoupled constant-parameter VBR model capable of studying motor-converter interactions in the range from dc to 10 MHz. Computer simulations and experimental studies of the VFD systems demonstrate that the proposed models represent advantages over existing/conventional models. It is also envisioned that proposed models will become a valuable asset for offline and real-time EMT simulators that are used for transient studies of machine-converter interactions in marine power systems, mining and oil drilling sites, and other applications with VFD systems.

Lay Summary

The induction machines and variable frequency drives (VFDs) are essential components of energy conversion in industrial and commercial applications/products. Modelling and simulating such motor-drive systems is essential for designing and operating all such applications and products. However, the existing models present a computational bottleneck and do not cover all phenomena needed for studying motor-converter interactions in modern electromagnetic transient (EMT) simulation tools.

This thesis advances the state-of-the-art modelling of these motor-drive systems by proposing new models that offer significant advantages over the previous models. It is envisioned that the new models will benefit the researchers and engineers who are performing simulation studies of VFD-based systems more efficiently, with higher accuracy, using less computational resources and time.

Preface

I confirm that I am the primary researcher responsible for the work presented in this thesis. Most of the research findings included in this thesis have been published in IEEE conference proceedings or will be submitted to an IEEE journal. In these publications, my responsibilities included developing mathematical models, analyzing approaches and data, conducting computer simulations, verifying results, and initiating and drafting papers. My supervisor, Dr. Juri Jatskevich, has provided invaluable guidance and constructive feedback throughout my research in the papers and this thesis. The co-authors of my conference publications, Mr. Taleb Vahabzadeh and Dr. Seyyedmilad Ebrahimi have also provided constructive feedback and comments and helped me refine the writing and presentation of the papers. The additional co-authors of my journal publication, Dr. Liwei Wang and Mr. Aria Fani, from UBC Okanagan, have provided some of the results from their experimental setup and helped in their interpretation and analysis used in the last manuscript. The specific publications from my thesis include the following:

Chapter 2 is based on the following conference paper that has been published:

S. Baig, S. Ebrahimi, and J. Jatskevich, “Efficient modeling of adjustable speed drive systems for offline and real-time EMT simulators,” in *Proc. IEEE 22nd Int. Symp. INFOTEH-JAHORINA (INFOTEH) Conf.*, East Sarajevo, Bosnia and Herzegovina, Mar. 15–17, 2023, pp. 1–6.

Chapter 3 is based on the following conference paper that has been published:

S. Baig, T. Vahabzadeh, S. Ebrahimi, and J. Jatskevich, “Reconfigurable star-delta VBR induction machine model for predicting soft-starting transients,” in *Proc. IEEE Int. IOT. Electron. Mech. (IEMTRONICS) Conf.*, Toronto, ON, Canada, Jun. 1–4, 2022, pp. 1–7.

Chapter 4 is based on the following journal article that is to be submitted:

S. Baig, S. Ebrahimi, J. Jatskevich, L. Wang, and A. Fani, “Wideband constant-parameter voltage-behind-reactance model of squirrel-cage induction machines,” (to be submitted), pp. 1–10.

Table of Contents

Abstract.....	iii
Lay Summary	iv
Preface.....	v
Table of Contents	vii
List of Tables	x
List of Figures.....	xi
List of Symbols	xv
List of Abbreviations	xvii
Acknowledgements	xviii
Dedication	xx
Chapter 1: Introduction	1
1.1 Motivation.....	1
1.2 Literature Review.....	2
1.3 Research Objectives.....	5
1.3.1 Objective I: Develop an efficient modelling approach for the simulation of adjustable speed drive systems in offline and real-time EMT programs.....	7
1.3.2 Objective II: Develop a reconfigurable star-delta VBR induction machine model for predicting soft-starting transients.....	7
1.3.3 Objective III: Develop a wideband constant-parameter voltage-behind-reactance model of squirrel-cage induction machines	8
Chapter 2: Efficient Modelling of Variable Frequency Drive Systems for Offline and Real-Time EMT Simulators	10

2.1	Modelling of Induction Motor Drive System	11
2.1.1	Average-Value Model (AVM) of VSI [46]	12
2.1.2	DCPVBR Model for the IM [18]	14
2.1.3	Volts-per-Hertz Control [17]	17
2.1.4	Machine-Converter Model Implementation	18
2.2	Computer Studies	21
2.2.1	Transient Study	22
2.2.2	Solution Accuracy	24
2.2.3	Computational Performance	26
Chapter 3: Reconfigurable Star-Delta VBR Induction Machine Model for Predicting Soft-		
Starting Transients		30
3.1	VBR Formulation with Variable Rotor Resistance	31
3.2	Simulation Studies	37
3.2.1	DOL Starting of Delta-connected Motor	39
3.2.2	Wye/Delta Starting of SCIM	42
3.2.3	Computational Performance	45
Chapter 4: Wide-Band Constant-Parameter Voltage-Behind-Reactance Model of Squirrel-		
Cage Induction Machines.....		48
4.1	Modelling of Induction Machine	49
4.1.1	Low-Frequency DCPVBR Model [18]	50
4.1.2	Universal High-Frequency Model [7]	53
4.1.3	High-Frequency Bearing Circuit Model [38], [39]	56
4.1.4	Proposed Wide-Band DCPVBR Model	58

4.2	Model Validation	60
4.2.1	Experimental Verification of DM and CM Impedances	61
4.2.2	High-Frequency DM and CM Analysis in VFD System	65
4.2.3	Reflected Over-Voltage Analysis in Long-Cable Fed IM Drive System	70
Chapter 5: Conclusion		74
5.1	Contributions	74
5.2	Anticipated Impact	78
5.3	Future Work	79
Bibliography		81
Appendices		88
Appendix A : Parameters for Case Study System of Section 2.2		88
Appendix B : Parameters for Case Study System of Section 3.2		89
Appendix C : Parameters for Case Study System of Section 4.2		90

List of Tables

Table 1.1 Summary of features of existing state-of-the-art models of three-phase induction machine in SVB EMT simulation programs.....	6
Table 2.1 Offline and real-time simulation performance comparisons of the subject models for the 6-second transient study with <i>ode4</i> solver	26
Table 3.1 Computational performance comparisons of the subject models for the 4-second wye-delta starting transient case study using non-stiff <i>ode45</i> and stiff <i>ode23tb</i> variable time-step solvers	46
Table 3.2 Computational performance comparisons of the subject models for the 4-second wye-delta starting transient case study using <i>ode3</i> fixed time-step solver	46
Table 5.1 Summary of features of the proposed induction machine model with respect to the existing state-of-the-art models.....	77

List of Figures

Figure 2.1 A typical VFD system consisting of a DC source, filter, VSI, short AC cable line, three-phase IM connected to compressor load, and V/Hz controller.....	11
Figure 2.2 Implementation of the AVM of VSI using dependent voltage/current sources: (a) AVM VSI in abc coordinates (b) AVM VSI in qd coordinates.	14
Figure 2.3 Implementation of the DCPVBR model of a three-phase Y-connected IM in an arbitrary reference frame.....	17
Figure 2.4 Implementation of the closed-loop Volts-per-Hertz (V/Hz) controller utilizing synchronous regulator and speed sensor measurement.	18
Figure 2.5 Interfacing of the AVMs of VSI with different models of IM: (a) DI-AVM VSI – qd IM (Direct interface in qd coordinates); (b) AVM VSI – Simscape Electrical built-in qd IM (Indirect interface in abc phase coordinates with snubbers); (c) AVM VSI – DCPVBR IM model (efficient interface in abc phase coordinates without snubbers).....	20
Figure 2.6 Implementation of subject models in offline and OPALRT5700 HIL real-time simulators using Simulink/RTLAB software.....	21
Figure 2.7 Transient response of system variables as produced by the subject models with $\Delta t = 5 \mu\text{s}$: (a) v_{as} , (b) i_{as} , (c) T_e , and (d) ω_{rm}	23
Figure 2.8 Magnified view of several variables from Figure 2.7, as obtained by the subject models with $\Delta t = 200 \mu\text{s}$: (a) v_{as} , (b) i_{as} , and (c) T_e	24
Figure 2.9 2-norm error of the subject models over 6 s transient case study with several different time-step sizes:(a) 2-norm phase “a” current error, (b) 2-norm phase “a” voltage error.	25
Figure 2.10 Snapshot depicting the percentage CPU utilization of proposed VSI–DCPVBR IM model executed on OPALRT 5700 simulator with $300\mu\text{s}$	29

Figure 3.1 Classical $qd0$ equivalent circuit in arbitrary reference frame for a three-phase squirrel-cage induction machine.....	32
Figure 3.2 Implementation of CPVBR–II model of a three-phase squirrel-cage induction machine for reconfigurable wye- and delta-connected stator windings.....	37
Figure 3.3 The test system consisting of a three-phase squirrel-cage induction machine connected to a power grid through power cables: (a) wye-connected machine, and (b) delta-connected machine.....	38
Figure 3.4 Implementation of qd model of a three-phase squirrel-cage induction machine for wye-connected and delta-connected stator windings.....	39
Figure 3.5 Transient response of system variables of Δ -connected IM as obtained by the subject models during start-up followed by a load change: (a) $v_{ab,line}$, (b) $v_{ag,phase}$, (c) $i_{as,line}$, (d) $i_{as,phase}$, (e) w_m , and (f) T_e	40
Figure 3.6 Magnified plots of selected variables during start-up of Δ -connected IM: (a) RMS line voltage $v_{ab,rms}$, (b) line current $i_{as,line}$, and (c) electromagnetic torque T_e	41
Figure 3.7 Transient response of system variables of Y- Δ starter-based IM as obtained by the subject models during start-up followed by Y- Δ switching and load change: (a) $v_{ab,line}$, (b) $v_{ag,phase}$, (c) $i_{as,line}$, (d) $i_{as,phase}$, (e) w_m , and (f) T_e	43
Figure 3.8 Magnified views of selected variables under: (a), (c), and (e) wye-connected IM starting condition; and (b), (d), and (f) Y- Δ switching transition.....	44
Figure 4.1 Typical three-phase VFD system consisting of a line-commutated rectifier (LCR) and a voltage-source-inverter (VSI), feeding a squirrel-cage induction motor (SCIM) through a power cable.....	49

Figure 4.2 Implementation of the DCPVBR model of a three-phase Y-connected IM with decoupled and constant RL branches for stator interfacing circuit [18].	52
Figure 4.3 Per-phase equivalent circuit representations of the universal high-frequency induction machine model [7] for arbitrary stator windings connections.	53
Figure 4.4 Setup arrangement for measuring the impedance characteristics of a three-phase squirrel-cage IM: (a) DM impedance (Z_{DM}) (b) CM impedance (Z_{CM}).	55
Figure 4.5 The differential and common mode universal high-frequency equivalent circuits of the induction machine (a) DM equivalent circuit (b) CM equivalent circuit.	56
Figure 4.6 High-Frequency bearing phenomenon (a) cross-section of electrical machine depicting induced bearing voltage and currents (b) equivalent high-frequency bearing circuit model [38], [39]	57
Figure 4.7 Implementation of the proposed WBDCPVBR model of induction machines augmented with bearing circuit model.....	59
Figure 4.8 Experimental laboratory setup of the VFD system: (1) ABB ACS150 drive with safety block, (2) power cable, (3) three-phase 7.5hp Baldor EM3710T IM with arbitrary stator windings connections and terminal voltages measurement setup, (4) bearing voltages measurement setup; (5) oscilloscope for displaying and recording output waveforms; (6) phase and CM currents measurement setup.....	61
Figure 4.9 Superimposed measured and simulated DM impedance characteristics of the proposed WBDCPVBR model for series-Y winding connection: (a) DM Magnitude, and (b) DM Phase. 62	
Figure 4.10 Superimposed measured and simulated CM impedance characteristics of the proposed WBDCPVBR model for series-Y winding connection: (a) CM Magnitude, and (b) CM Phase.	63

Figure 4.11 Response of several system variables as obtained by the experimental measurements and proposed model under no-load condition for 1m power cable: (a) v_{ag} , (b) v_{ab} , (c) i_{as} , (d) v_{ng} , (e) v_B , and (f) i_{CM}	66
Figure 4.12 Magnified view of the corresponding variables from Figure 4.11 as obtained by the experimental measurements and proposed model under no-load condition for 1m power cable: (a) v_{ng} , (b) v_B , and (c) i_{CM}	67
Figure 4.13 CM and DM response of parallel-Y IM configuration as obtained by the experimental measurements and proposed WBDCPVBR model under no-load condition for 1m power cable: (a) v_{CM} , (b) i_{CM} , (c) v_{DM} , and (d) i_{DM}	68
Figure 4.14 Measured reflected over-voltage waveforms at the motor terminals and bearing/shaft when using 50m power cable.....	70
Figure 4.15 Reflected over-voltage waveforms at the motor terminals and bearing/shaft for 50m power cable as obtained by the proposed model: (a) v_{ag} , (b) v_{bg} , (c) v_{cg} , (d) v_{ng} , and (e) v_B	72

List of Symbols

Throughout this thesis, scalar quantities are specified by italic letters, e.g. v_{as} , vectors are specified by lower-case bold letters, e.g. \mathbf{v}_{abc} , and matrices are specified by upper-case bold letters, e.g. $\mathbf{K}_s(\theta)$. For compactness of equations and notations, variables can be grouped together in the following form:

$$\mathbf{f}_{abcx} = [f_{ax} \quad f_{bx} \quad f_{cx}]^T, \quad \mathbf{f}_{qd0x} = [f_{qx} \quad f_{dx} \quad f_{0x}]^T, \quad \text{and } x = s, r,$$

where f may denote voltage (v), current (i), and flux linkage (λ), s stands for the stator, and r stands for the rotor of the electrical machine. For modelling purposes, the rotor variables are rescaled by the appropriate turns ratio to the stator side, and motor sign convention is considered.

This section only presents fundamental variables, while all other variables are explicitly defined throughout the thesis.

$e''_{as}, e''_{bs}, e''_{cs}$	Phase a , b , and c sub-transient back-emf voltages
i_{as}, i_{bs}, i_{cs}	Stator phase a , b , and c currents
i_{qr}, i_{dr}	q -axis, and d -axis rotor currents
i_{qs}, i_{ds}, i_{0s}	Stator q -axis, d -axis, and zero-sequence currents
J	Combined moment of inertia of machine and load
$\mathbf{K}_s(\theta), \mathbf{K}_s^{-1}(\theta)$	Park's transformation and inverse transformation matrices
L_m	Magnetizing inductance

M	Modulation index
p	Heaviside's derivative operator
P	Number of poles
r_r, L_{lr}	Rotor resistance and leakage inductance
r_s, L_{ls}	Stator resistance and leakage inductance
T_e	Electromagnetic torque
T_m	Mechanical torque
T_{sw}, f_{sw}	VSC's switching interval and switching frequency
v_{as}, v_{bs}, v_{cs}	Stator phase $a, b,$ and c voltages
V_{dc}	DC voltage source
v_{qs}, v_{ds}, v_{0s}	q -axis, d -axis, and zero-sequence stator voltages
θ_c	Converter reference frame angle
θ_s	Synchronous reference frame angle
$\lambda_{as}, \lambda_{bs}, \lambda_{cs}$	Stator phase $a, b,$ and c flux linkages
$\lambda_{mq}, \lambda_{md}$	q -axis, and d -axis magnetizing flux linkages
$\lambda_{qr}, \lambda_{dr}$	q -axis, and d -axis rotor flux linkages
Δt	Time step size
ω_r, θ_r	Electrical rotor speed (in rad/s) and position (in rad)
ϕ	Power factor angle

List of Abbreviations

AC	Alternating current
ASD	Adjustable speed drive
AVM	Average-value model
CM	Common-mode
CPVBR	Constant-parameter voltage-behind-reactance (model)
DC	Direct current
DM	Differential-mode
EMI	Electromagnetic interference
EMT	Electromagnetic transient
EMTP-type	Nodal-equations-based programs
HF	High-frequency
IM	Induction machine
LCR	Line commutated rectifier
LF	Low-frequency
PD	Phase-domain (model)
<i>q</i> - and <i>d</i> - axes	Quadrature and direct axes
SVB	State-variable-based (simulation program)
VFD	Variable frequency drive
VSI	Voltage source inverter
WBDCPVBR	Wide-band decoupled constant-parameter VBR (model)

Acknowledgements

I want to express my sincere appreciation to my research supervisor, Dr. Juri Jatskevich, for his excellent academic guidance, profound wisdom, constructive feedback and comments, insightful discussions, dedication, inspiration, and unwavering support throughout my MASc program. Dr. Juri Jatskevich's collective efforts helped me realize this thesis and its contributions. The knowledge and skills I acquired through his excellent supervision will contribute to my professional career success. I would also thank Dr. Jatskevich for providing additional funding through the Natural Science and Engineering Research Council (NSERC) under the Discovery Grant entitled "Modeling and Analysis of Power Electronic and Energy Conversion Systems" and under the Alliance Grant entitled "Integrated Design and Operation of Hybrid-electric Shipboard Systems," without which this research would not have been possible. I also profoundly thank Dr. Seyyedmilad Ebrahimi for his mentorship, guidance, valuable feedback, and comments on my research projects.

I also want to thank the examining committee members, Dr. Hermann Dommel and Dr. Christine Chen, for dedicating their valuable time and providing useful comments and feedback to improve my thesis. I also thank Dr. Liwei Wang and Mr. Aria Fani, from UBC Okanagan, for providing some of the results from their experimental setup and for their help in the interpretation and analysis used in the last manuscript.

Also, I owe special thanks to the faculty, staff, friends, and colleagues in the Electrical Power and Energy System Group at UBC for all the help and support throughout my studies. Specifically, I am deeply thankful to Taleb Vahabzadeh, Arash Safavizadeh, Erfan Mostajeran, Gloria Wang, Parastoo Hosseinian, Jinhe Zhou, Levi Bieber, Ziliang Feng, Rahul Ramesh,

Ekamjot Tahim, Zhenyao Sun, Javier Tarazona, and many others for the helpful discussions, inspiring working environment, and enjoyable time in our laboratory. Particularly, I want to thank Taleb Vahabzadeh for his genuine friendship, valuable feedback, and discussions on the papers we co-authored.

Lastly, I express my deepest gratitude to my dear parents, Azhar and Nabila, for their unconditional love and support throughout my academic pursuits and life. Additionally, I express my appreciation to my three siblings, Suleman, Afshan, and Wajahat, for their encouragement and support.

Dedication

To my wonderful family for their unconditional love and support

Chapter 1: Introduction

1.1 Motivation

Induction machines (IMs) have been essential components in electromechanical energy conversion accounting for 60-70% of the energy consumed in the power grid [1]. Due to their simple design, low cost, reliability, robustness, and self-starting capability, squirrel-cage induction machines have been widely used in many commercial and industrial applications such as conveyor belts, pumps, mills, crushers, drilling machines, centrifugal machines, etc. [2]–[5]. The induction machines are also commonly used as motors in vehicular and marine applications as propulsors and auxiliary services, where they are also inverter-controlled [6].

In IMs, energy conversion is mainly achieved through air-gap flux created by stator and rotor currents. Additionally, IMs can be configured in different stator winding connections based on performance requirements and application needs [7], [8], with star (Y) and delta (Δ) being common choices. However, some challenges are associated with the direct line starting of induction motors, including high starting currents, torque pulsations, and large reactive power, which increases the stresses on power system components, causing voltage drops across the power system. To overcome these challenges, various soft-starting methods have been introduced, which include star-delta starting, auto-transformer starting, AC voltage regulators, variable frequency drives (VFDs), microcontroller-based starters, [9], [10], etc. In the VFD-based systems, squirrel-cage induction machines fed from inverters through power cables are utilized in many commercial and industrial applications, such as in offshore platforms, mining, oil and gas drilling, automotive, marine propulsion, aerospace, railway traction, hybrid/fully electric vehicle systems [11]–[14], etc.

Modelling of IMs and VFD systems has been essential for designing, tuning, and operating all electrical systems with motors and generators.

Electromagnetic transient (EMT) simulation programs are considered indispensable tools for offline and real-time simulation studies to analyze the electromechanical and electromagnetic transients in motor drive applications. The EMT simulation programs can be broadly categorized into two groups, i.e. nodal-equation-based (EMTP-type) and state-variable-based (SVB) programs. The SVB EMT programs generate a set of differential-algebraic equations in a state-state form which are discretized and numerically solved at the system level using either fixed- or variable-time-step solvers. This thesis considers IM models for the SVB EMT programs only, whereas the extension of the work to EMTP-type simulators represents future research.

1.2 Literature Review

Modelling of IMs has been active research over the past few decades due to the increasing utilization of electrical energy in many applications. Depending on the required fidelity level, study objectives, and frequency range of interest, several classes of models of induction machines have been proposed in the literature. For instance, in the low-frequency range (dc to ~ 10 kHz), induction machines mainly exhibit inductive behaviour and can be represented by the so-called lumped-parameter low-frequency models, including the phase domain (PD) [15], [16], classical $qd0$ [17], and voltage-behind reactance (VBR) [18] models. The PD model yields rotor position-dependent and time-varying inductances, which thus make it computationally expensive for system-level studies [19]. While the $qd0$ model offers constant and decoupled inductances, resulting in more straightforward implementation, it encounters issues of numerical error and simulation

inefficiency due to its indirect interface with inductive and switching power networks using artificial snubbers [19] in SVB EMT simulation programs.

To overcome the interfacing problem, constant-parameter voltage-behind-reactance (CPVBR) models were proposed in [18], which represent the stator interfacing circuit as three-phase controlled voltage sources behind RL branches in abc phase coordinates and the rotor subsystem in qd coordinates with rotor flux linkages as state-variables. All CPVBR models allow direct interface with arbitrary inductive or switching circuits without snubber circuits. Furthermore, the CPVBR models are capable of representing both star (Y) and delta (Δ) stator winding connections. Consequently, the CPVBR models offer significant advantageous features and are well-suited for system-level studies [18].

Furthermore, it was shown in [20] that $qd0$ model underestimate the current switching ripples in machine-drive interaction studies. Induction machine behaviour becomes more capacitive in the high-frequency range, which is attributed to the increasing influence of stray capacitances between the stator winding and motor frame [21]–[24]. To study the high-frequency phenomena, numerous high-frequency models of induction machines [7], [12], [21], [24]–[34] were developed using the differential-mode (DM) and common-mode (CM) impedance measurements of the machine in the frequency domain. Such models, also known as high-frequency behavioural circuit models, are primarily established to characterize machine behaviour at higher frequencies. The high-frequency behavioural models [12], [25]–[28] also have high-order and complex structures and require complicated parameterization procedures.

To address these challenges, researchers concentrated on developing relatively simple and easily parametrizable high-frequency models, which encompass single- [24], [30], [31] or multiple- [28], [29] section phase-belt winding models. In [7], a universal high-frequency model

was proposed by leveraging the single-section phase-belt winding model [31] and extending the high-frequency model developed in [34]. Specifically, this universal high-frequency model [7] features a relatively simple and unified structure capable of representing arbitrary, i.e. Y-, Δ -, series- and parallel-stator windings connections. Moreover, this model demonstrates accuracy in the mid-high frequency range (i.e., 50kHz to 10MHz) and presents a straightforward parametrization procedure.

Furthermore, it should be noted that bearing voltages are also induced in the machine through stray capacitances leading to discharging bearing currents under the high-frequency PWM operation of the VFDs [32], [35]. To study such a phenomenon, researchers have proposed several high-frequency bearing equivalent circuit models [21], [32], [35]–[41] in the literature. In [39], a capacitive voltage divider circuit model consisting of several stray capacitances was proposed to capture the induced bearing voltages. However, CM equivalent circuit models can be employed [21] to study such effects as bearing voltages are correlated with the induced CM voltages and the resultant CM currents flow [35], [41]. It should also be mentioned that the DM and CM models of IM proposed in the literature address only the limited high-frequency EMI phenomena [21], [33]. In addition, a subset of these developed high-frequency models utilize parameters that lack direct correlation to the geometry and physical behaviour of the machine [21].

Concurrently, a strong need exists to integrate the low- and high-frequency machine models, thus facilitating a comprehensive representation of induction machine behaviour across a broad frequency spectrum for VFD applications. Furthermore, including motor slip variations in the high-frequency models would enable the examination of low-frequency electromechanical transients in the machines, which the low-frequency models optimally predict [15]–[18]. Considering this objective, a methodology was developed in [42] wherein a high-frequency

distributed circuit model was connected in parallel to the classical $qd0$ model using a high-pass filter. However, due to the use of a high-pass filter, inaccuracies in the model results could occur. In [12], a three-phase model was developed by taking into account the inductive and capacitive coupling between the stator phases and ground, which resulted in high order model structure and its complicated characterization. In [21], a three-phase model was proposed by combining the IEEE recommended steady state T-circuit model [43] with high-frequency branches to represent the low-high frequency response characteristics of IM. However, it should be noted that the T-equivalent circuit model is a reduced-order steady-state model, which does not accurately represent the machine's low-frequency dynamic behaviour [7]. At the same time, some full-order IM models [20], [44] were developed, focusing on representing its dynamic behaviour by utilizing the distributed rotor circuit along with machine flux saturation for enhanced accuracy. However, such models were primarily focused on representing machine behaviour within low-mid frequencies below 50 kHz. In [20], an advanced full-order $qd0$ model was proposed, which took into account main and leakage flux saturation as well as distributed rotor circuit. However, the inclusion of a high-order rotor transfer function led to increased structural complexity, model parameters, and complicated characterization, which introduced practical challenges [45].

1.3 Research Objectives

The main objectives of this research work are to advance the state-of-the-art modelling of induction machine-converter systems for their accurate and efficient simulations in EMT programs. For the research framework, I chose the VBR model formulation due to its advantageous features that are particularly useful for interfacing the machine model with models of power electronic converters and the ability to reconfigure the stator windings into Y and Δ connections

as may be required for various motor-drive applications. A suitable machine model is highly desirable to study the motor-converter interactions, bearing currents, over-voltages, and EMI in a wide range of frequencies. In this regard, the considered VBR modelling approach also has advantages as it may be combined with other models designed to capture the corresponding high-frequency phenomena. The scope of this thesis is also limited to implementing the proposed models in the state-variable-based (SVB) EMT simulation programs, whereas the extension of the models to the nodal-based EMTP-type programs is considered future research. The features of the most relevant existing state-of-the-art induction machine models are summarized in Table 1.1.

With respect to the prior models, my research is focused on the following three objectives:

Table 1.1 Summary of features of existing state-of-the-art models of three-phase induction machine in SVB EMT simulation programs

Models	PD [15],[16]	$qd0$ [17]	VBR [18]	[12], [25]– [28]	[20]	[7]	[21]	
Structure	complex	simple	simple	complex	complex	simple	complex	
Interfacing circuit	variable & direct	constant & indirect	constant & direct	constant & direct	constant & indirect	constant & direct	constant & direct	
Parameterization method	easy	easy	easy	complicated	complicated	easy	complicated	
Valid frequency range (Hz)	~DC-5k	~DC-5k	~DC-5k	~5k~10M	~1k~50k	50k-10M	10-10M	
Low-frequency behaviour	Transient	Yes	Yes	Yes	No	Yes	No	No
	Steady-state	Yes	Yes	Yes	No	Yes	No	Yes
	Motor slip variation	Yes	Yes	Yes	No	Yes	No	Yes
High-frequency behaviour	Transient	No	No	No	Yes	Yes	Yes	Yes
	Steady-state	No	No	No	Yes	Yes	Yes	Yes
	DM impedance	low-freq. range	low-freq. range	low-freq. range	mid-high freq. range	–	mid-high freq. range	low-high freq. range
	CM impedance	No	No	No	Yes	–	Yes	Yes
	CM current	No	No	No	–	–	No	No
	Reflected over-voltages	No	No	No	Yes	–	Yes	Yes
	Bearing voltages	No	No	No	No	No	No	Yes

1.3.1 Objective I: Develop an efficient modelling approach for the simulation of adjustable speed drive systems in offline and real-time EMT programs

It is demonstrated in Table 1.1 that the VBR models offer the capability of direct and efficient interfacing with arbitrary inductive or switching networks without the need for artificial snubber circuits, thus making the VBR models useful for system-level studies of variable frequency drives (VFDs). Additionally, the average-value models (AVMs) of voltage source converters (VSCs) offer significant computational advantages over using detailed switching models for system-level studies. The AVMs with VBR machine models are particularly suitable for system-level studies of marine power and propulsion systems, where several motors and converters are utilized together with many other electromechanical components. Therefore, the first objective of this thesis is to develop and implement the most efficient modelling approach for real-time and offline simulations of VFD systems. Specifically, the numerical performance of several combinations of machine-converter models is investigated. This is achieved by utilizing a detailed switching model and AVM for the voltage source inverter (VSI) in conjunction with the $qd0$ and DCPVBR models for the induction machine. Through rigorous simulation analysis, the research identifies the best combination of machine and converter models (and their interfacing) for system-level studies of VFDs in offline and real-time EMT simulators.

1.3.2 Objective II: Develop a reconfigurable star-delta VBR induction machine model for predicting soft-starting transients

In some applications, the induction motors are switched between the Y and Δ connections during their starting and subsequent operation in order to minimize transient currents and optimize

energy conversion during regular operation. Such applications commonly include large machinery in factories and medium-sized marine systems (from 10kW to several MW). Developing models for such reconfigurable applications is highly desirable since the conventional $qd0$ models are not well suited. As an extension of the research work on the state-of-the-art VBR modelling, the reconfigurable star-delta constant-parameter voltage-behind-reactance (CPVBR) model of a three-phase squirrel-cage induction machine is presented. This objective is achieved by utilizing the advantageous properties of the CPVBR model (which has access to all six stator winding terminals) to switch between star and delta configurations during the run-time. This feature has not been utilized previously in the literature. In addition, the low-frequency deep-rotor-bar phenomenon is also incorporated into the model for enhanced accuracy in representing the transient phenomenon during motor starting. The presented model provides accurate predictions of transient responses during motor starting, star-delta switching transitions, and steady-state operation with either stator winding connection.

1.3.3 Objective III: Develop a wideband constant-parameter voltage-behind-reactance model of squirrel-cage induction machines

It is shown in Table 1.1 that conventional PD, $qd0$, and VBR models are capable of accurately predicting steady-state, electromechanical, and electromagnetic transients behaviour in the low-frequency range (i.e., up to several kHz). However, these models do not represent the machine impedance characteristics and any effects in the mid-high frequency range (i.e., several kHz to 10 MHz). Some of the high-frequency IM models as illustrated in Table 1.1. offer limited scope and capabilities in predicting mid-to-high frequency phenomena. Also, such models typically feature complex structures and complicated parameterization methods. Moreover, these

high-frequency models do not predict low-frequency electromagnetic transients and motor slip variations. To bridge the gap in existing induction models, it is desirable to have a model capable of capturing all transient phenomena in the range from dc to 10 MHz and can be effectively used for the analysis of VFD systems. This objective is achieved by proposing a wideband decoupled constant-parameter VBR (WBDCPVBR) model for Y-connected squirrel-cage IM, which predicts the CM and DM impedances and currents, reflected transient over-voltages across the motor terminals, motor loading effects, and bearing voltages and currents. A model with such capabilities is required to study the machine-converter interactions and bearing currents in marine propulsion applications, where it is critical to design controllers and mitigating measures to reduce all parasitic currents that contribute to premature corrosion and equipment lifespan reduction. To my knowledge, a model with this collection of features has not been proposed in the prior literature.

Chapter 2: Efficient Modelling of Variable Frequency Drive Systems for Offline and Real-Time EMT Simulators

Variable frequency drives (VFDs) comprised of inverter-driven induction machines have been increasingly used in many energy conversion applications [2]. Design and analysis of such systems require accurate and efficient models of induction machines (IM) and voltage source inverters (VSI). Usually, simulations of such systems are carried out using detailed switching models of VSI and qd IM models, which are readily available as built-in library components in many electromagnetic transient (EMT) simulation programs. However, detailed switching models of converters with qd IM models typically require interfacing snubbers and small time steps, making them computationally expensive. For many system-level studies, the average-value models of the VSIs may be used more effectively. Also, the VBR machine models may offer some advantages in terms of interfacing with converter circuits.

This chapter presents an efficient modelling approach for VFD simulations using the average-value model of VSI [46] and decoupled constant-parameter voltage-behind-reactance (DCPVBR) model [18] of IM. The numerical performance of several combinations of machine-converter models is also investigated for efficient implementation of VFD systems in offline and real-time simulators. The computational performance of the presented models and the advantages of the proposed modelling method over existing approaches have been verified through simulation studies carried out using MATLAB-Simulink [47] and the real-time OPALRT5700 [48] simulator.

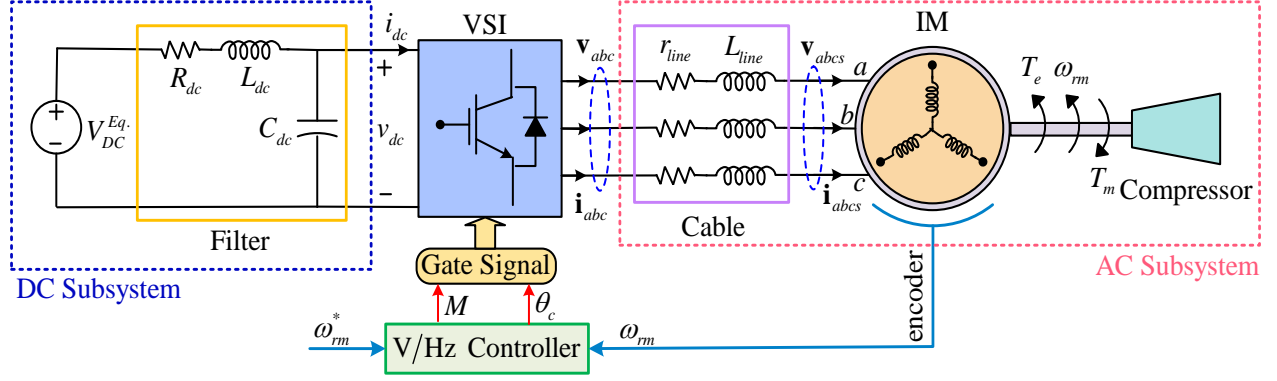


Figure 2.1 A typical VFD system consisting of a DC source, filter, VSI, short AC cable line, three-phase IM connected to compressor load, and V/Hz controller.

2.1 Modelling of Induction Motor Drive System

A typical induction motor drive system shown in Figure 2.1 is considered, wherein a VSI drives a three-phase squirrel-cage IM through cables. Without loss of generality, the mechanical load is represented in Figure 2.1 as a compressor coupled with the motor shaft. The VSI is assumed to be fed through a filter from a DC power source.

The system variables can be transformed from abc to qd coordinates and vice-versa as follows

$$\mathbf{f}_{qd} = \mathbf{K}(\theta)\mathbf{f}_{abc}, \quad \mathbf{f}_{abc} = \mathbf{K}^{-1}(\theta)\mathbf{f}_{qd}, \quad (2.1)$$

where

$$\mathbf{f}_{abc} = [f_a \quad f_b \quad f_c]^T, \quad \mathbf{f}_{qd} = [f_q \quad f_d]^T. \quad (2.2)$$

Here, omitting the zero sequence, θ represents the reference frame angle which can be the converter reference frame angle (θ_c) used for VSI or the arbitrary reference frame angle (θ) used

for IM. Whereas, $\mathbf{K}(\theta)$ and $\mathbf{K}^{-1}(\theta)$ are Park's transformation and inverse transformation matrices [17], herein defined without the zero sequence as

$$\mathbf{K}(\theta) = \frac{2}{3} \begin{bmatrix} \cos(\theta) & \cos(\theta - 2\pi/3) & \cos(\theta + 2\pi/3) \\ \sin(\theta) & \sin(\theta - 2\pi/3) & \sin(\theta + 2\pi/3) \end{bmatrix}, \quad (2.3)$$

$$\mathbf{K}^{-1}(\theta) = \begin{bmatrix} \cos(\theta) & \sin(\theta) \\ \cos(\theta - 2\pi/3) & \sin(\theta - 2\pi/3) \\ \cos(\theta + 2\pi/3) & \sin(\theta + 2\pi/3) \end{bmatrix}. \quad (2.4)$$

2.1.1 Average-Value Model (AVM) of VSI [46]

To achieve significant computational advantages in offline/real-time simulations, the AVM formulation neglects discrete switching of the converter and establishes the relation between DC- and AC- side variables transformed in qd synchronous (converter) reference frame by performing fast averaging on them over the switching interval as follows [46]

$$\bar{g}(t) = \frac{1}{T_{sw}} \int_{t-T_{sw}}^t g(\tau) d\tau, \quad T_{sw} = \frac{1}{f_{sw}}, \quad (2.5)$$

where T_{sw} and f_{sw} represent the VSC's switching interval and switching frequency. The $\bar{g}(t)$ represents the average value of a signal which can be either current or voltage.

To develop the AVM, the fundamental components of AC currents are transformed into qd reference frame by using Park's transformation $\mathbf{K}(\theta_c)$, thus resulting in averaged $\bar{\mathbf{i}}_{qd}$ as

$$\bar{\mathbf{i}}_{qd} = \begin{bmatrix} \bar{i}_q \\ \bar{i}_d \end{bmatrix} = \mathbf{K}(\theta_c) [i_a \quad i_b \quad i_c]^T. \quad (2.6)$$

Assuming a lossless converter, the averaged DC current \bar{i}_{dc} is computed as

$$\bar{i}_{dc} = \left(\frac{3}{4} M \right) \|\bar{\mathbf{i}}_{qd}\| \cos \phi, \quad (2.7)$$

where modulation index M and power factor angle ϕ are defined by

$$M = \frac{\sqrt{v_q^{e*2} + v_d^{e*2}}}{(V_{dc}/2)}, \quad \phi = \tan^{-1} \left(\frac{\bar{i}_d}{\bar{i}_q} \right), \quad (2.8)$$

Herein, M is computed by assuming sinusoidal PWM, V_{dc} is the DC voltage source, v_q^{e*} and v_d^{e*} are the q - and d - axes command voltages coming from the volts-per-hertz controller. Using M , and \bar{v}_{dc} as inputs, the averaged $\bar{\mathbf{v}}_{qd}$ voltages are computed as

$$\bar{\mathbf{v}}_{qd} = \begin{bmatrix} \bar{v}_q \\ \bar{v}_d \end{bmatrix} = \left(\frac{1}{2} M \right) \bar{v}_{dc} \begin{bmatrix} 1 \\ 0 \end{bmatrix}. \quad (2.9)$$

The voltages in abc coordinates are obtained using inverse Park's transformation matrix $\mathbf{K}^{-1}(\theta_c)$ as

$$\mathbf{v}_{abc} = [v_a \quad v_b \quad v_c]^T = \mathbf{K}^{-1}(\theta_c) \begin{bmatrix} \bar{v}_q \\ \bar{v}_d \end{bmatrix}. \quad (2.10)$$

Finally, (2.6)–(2.10) constitute the AVIM of VSI in abc phase coordinates. The implementation of VSC AVIM in abc phase coordinates is done by using controlled voltages or current sources in EMT simulation programs, as illustrated in Figure 2.2(a). Therein, the dc voltage \bar{v}_{dc} and ac currents \mathbf{i}_{abc} are required as inputs to calculate the interfacing variables, i.e. dc current \bar{i}_{dc} and ac voltages \mathbf{v}_{abc} , simultaneously (which makes the formulation implicit). However, the solution can only be available at the next time step. This can be overcome by introducing a one-time step delay at the cost of compromising numerical accuracy and stability.

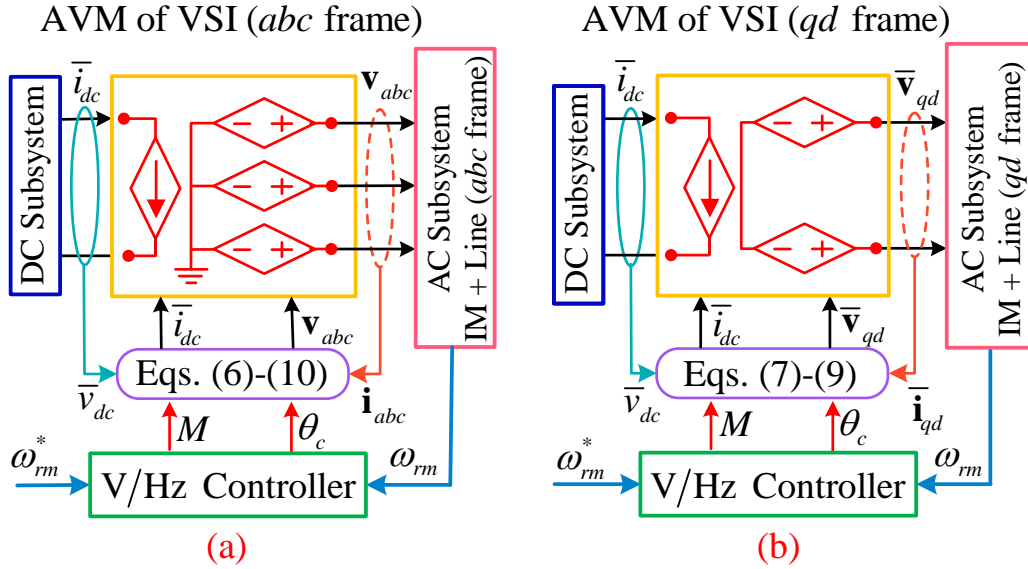


Figure 2.2 Implementation of the AVM of VSI using dependent voltage/current sources: (a) AVM VSI in abc coordinates (b) AVM VSI in qd coordinates.

An alternative solution is to implement the AVM directly in qd coordinates [see (2.7)–(2.9)] without adding one time-step delay to ensure numerical accuracy and stability, as depicted in Figure 2.2(b). To accomplish this, all external components connected to VSC also must be represented in qd frame. This would be the most computationally efficient and accurate solution, and because of this property, it is also considered the benchmark model in this Chapter 2.

2.1.2 DCPVBR Model for the IM [18]

The decoupled constant-parameter VBR formulation [18] is considered herein to obtain a direct interface with the VSI AVM. The VBR [18] is derived from the classical $qd0$ model [17]. The DCPVBR model is based on the coupled CPVBR [18] by assuming a Y-connected stator

winding and removing the off-diagonal terms. The final stator interfacing equation can be written as

$$\mathbf{v}_{abc} = r_D \mathbf{i}_{abc} + L_D p \mathbf{i}_{abc} + \mathbf{e}_{abc}'' \quad (2.11)$$

Here, \mathbf{v}_{abc} denotes the stator voltages, \mathbf{i}_{abc} denotes the stator currents, and \mathbf{e}_{abc}'' denotes the back-emf voltages in abc frame, respectively. The resistance r_D and inductance L_D are calculated as [18]

$$r_D = r_s + L_m''^2 L_{lr}^{-2} r_r, \quad L_D = L_{ls} + L_m'' \quad (2.12)$$

Here, r_s and L_{ls} are the stator resistance and leakage inductance, r_r and L_{lr} are the rotor resistance and leakage inductance. The so-called sub-transient inductance L_m'' can be defined as

$$L_m'' = (L_m^{-1} + L_{lr}^{-1})^{-1} \quad (2.13)$$

In (2.11), \mathbf{e}_{abc}'' is obtained as

$$\mathbf{e}_{abc}'' = \begin{bmatrix} e_{as}'' & e_{bs}'' & e_{cs}'' \end{bmatrix}^T = \mathbf{K}^{-1}(\theta) \begin{bmatrix} e_{qs}'' \\ e_{ds}'' \end{bmatrix}, \quad (2.14)$$

where

$$e_{qs}'' = \omega_r L_m'' L_{lr}^{-1} \lambda_{dr} + r_r L_m'' L_{lr}^{-2} (L_m'' L_{lr}^{-1} - 1) \lambda_{qr}, \quad (2.15)$$

$$e_{ds}'' = -\omega_r L_m'' L_{lr}^{-1} \lambda_{qr} + r_r L_m'' L_{lr}^{-2} (L_m'' L_{lr}^{-1} - 1) \lambda_{dr}. \quad (2.16)$$

The rotor flux linkages form the state equations for the rotor subsystem, which can be expressed as follows

$$p \lambda_{qr} = r_r L_{lr}^{-1} (L_m'' L_{lr}^{-1} - 1) \lambda_{qr} - (\omega - \omega_r) \lambda_{dr} + r_r L_{lr}^{-1} L_m'' i_{qs}, \quad (2.17)$$

$$p \lambda_{dr} = r_r L_{lr}^{-1} (L_m'' L_{lr}^{-1} - 1) \lambda_{dr} + (\omega - \omega_r) \lambda_{qr} + r_r L_{lr}^{-1} L_m'' i_{ds}. \quad (2.18)$$

Here p is the Heaviside derivative operator, i.e. $p = d/dt$, ω is the angular speed of the arbitrary reference frame, and ω_r is the angular speed of the rotor. In (2.17)–(2.18), \mathbf{i}_{qds} can be obtained as follows

$$\mathbf{i}_{qds} = \begin{bmatrix} i_{qs} \\ i_{ds} \end{bmatrix} = \mathbf{K}(\theta) [i_{as} \quad i_{bs} \quad i_{cs}]^T. \quad (2.19)$$

Finally, the developed electromagnetic torque and angular rotor speed are calculated as

$$T_e = \left(\frac{3P}{4} \right) \left(\frac{L_m''}{L_r} \right) (\lambda_{dr} i_{qs} - \lambda_{qr} i_{ds}), \quad (2.20)$$

$$p\omega_r = \frac{P}{2J} (T_e - T_m), \quad \omega_{rm} = \frac{2}{P} \omega_r, \quad (2.21)$$

where P denotes the number of poles, and J represents the moment of inertia.

The implementation of the DCPVBR model is demonstrated in Figure 2.3, wherein rotor flux linkages are used as state variables, and stator currents are used as inputs to calculate the sub-transient back-emf voltages in the stator interfacing circuit. Note that snubbers are not used here.

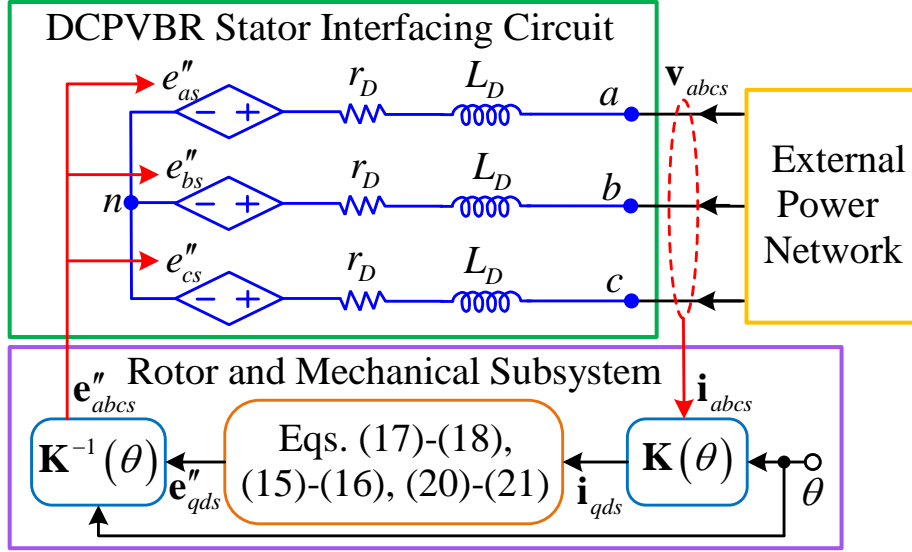


Figure 2.3 Implementation of the DCPVBR model of a three-phase Y-connected IM in an arbitrary reference frame.

2.1.3 Volts-per-Hertz Control [17]

The classical volts-per-hertz control is assumed here [17]. Herein, a closed-loop control utilizing a synchronous regulator with rotor speed sensor measurement is considered to accomplish variable speed operation with higher accuracy. For this purpose, the speed command ω_{rm}^* is typically used with a slew-rate limiter (SRL_a) to reduce speed transients and limit the speed command rate of change between α_{\min} and α_{\max} . However, the integrated error in speed is also set to limit between β_{\min} and β_{\max} . The synchronous regulator uses the command and measured rotor speeds ($\omega_{rm}^*, \omega_{rm}$) as inputs to calculate the modified speed input command ω_{rm}^{**} , which can be written as [17]

$$\omega_{rm}^{**} = \omega_{rm}^* + \frac{K_i}{s} (\omega_{rm}^* - \omega_{rm}) = \omega_{rm}^* + \frac{1}{\tau_{reg} s} (\omega_{rm}^* - \omega_{rm}). \quad (2.22)$$

Next, considering the number of poles, the command electrical speed ω_e^* and converter angle θ_c are expressed as

$$\omega_e^* = \frac{P}{2} \omega_m^*, \quad \theta_c = \int \omega_e^* dt. \quad (2.23)$$

Finally, the command q - and d - axes voltages are calculated as

$$v_q^{e*} = \left(\frac{\sqrt{2}V_b}{\omega_b} \right) \omega_e^*, \quad v_d^{e*} = 0, \quad (2.24)$$

where V_b is the base phase voltage, and ω_b is the base electrical frequency. The final considered V/Hz controller is depicted in Figure 2.4.

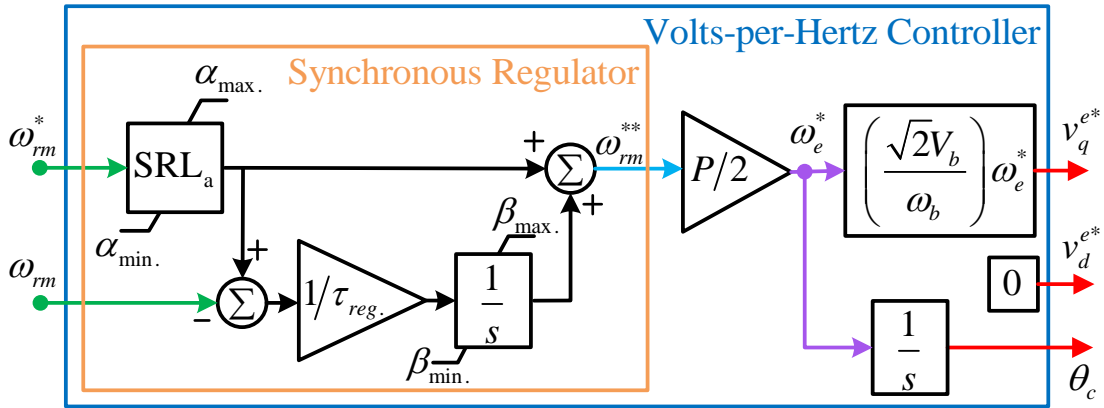


Figure 2.4 Implementation of the closed-loop Volts-per-Hertz (V/Hz) controller utilizing synchronous regulator and speed sensor measurement.

2.1.4 Machine-Converter Model Implementation

For the purpose of the computer studies, a total of five combinations of models are considered:

The first model considers the detailed switching VSI model and the Simscape Electrical (SE) built-in qd IM model. Since the qd IM cannot be interfaced directly with external inductive and switching circuits, therefore, shunt resistive snubbers of 785Ω are added in parallel to limit the solution error to 2%.

The second model considers the detailed switching VSI and the DCPVBR IM model, which are interfaced directly without artificial snubbers. However, it is worth noting that the detailed VSI model also contains internal shunt snubbers, which may limit computational efficiency.

The third model is the reference, which is composed of AVM of VSI with controlled voltages/current sources in qd coordinates for its direct interfacing with the qd IM model (developed using basic blocks of Simulink in qd coordinates). This combination does not require a time-step delay and/or snubbers. This reference model is used as a benchmark as it yields the most efficient and accurate solution (although it does not permit using the SE built-in qd model). To include the cable impedance, it was simply added to the IM model in stator branch parameters, which also makes this approach less practical (and not general) in EMT programs requiring the building of a custom qd IM model. The interfacing of AVMs of VSI with different models of IM is depicted in Figure 2.5.

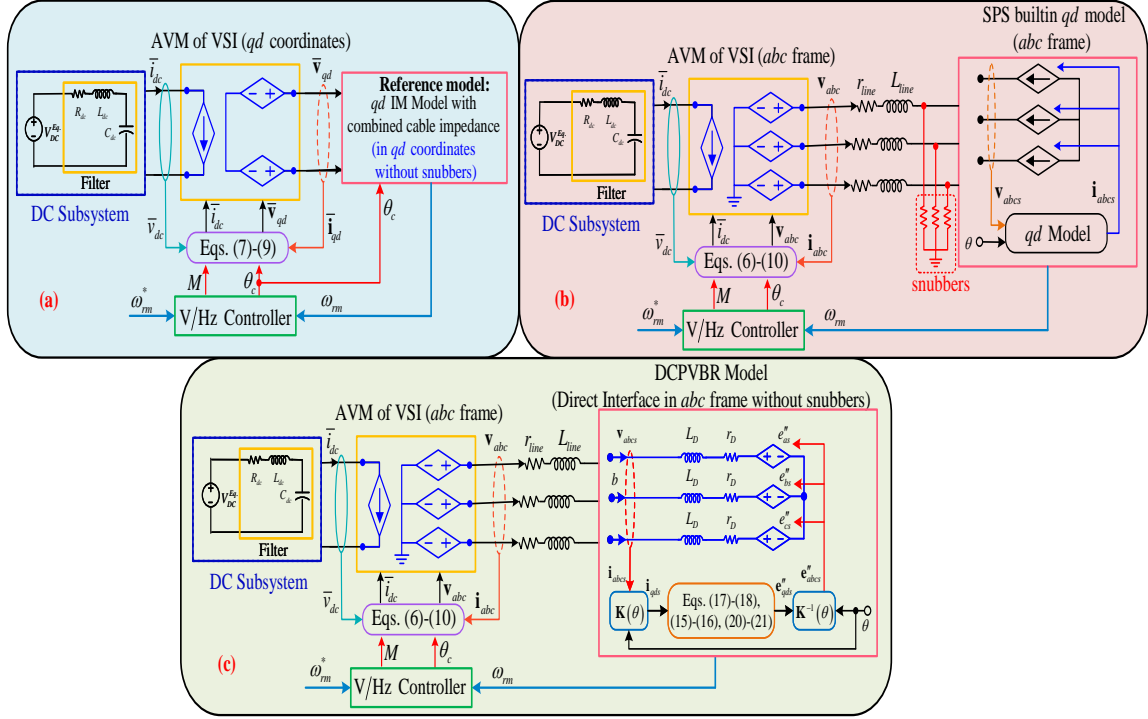


Figure 2.5 Interfacing of the AVMs of VSI with different models of IM: (a) DI-AVM VSI – qd IM (Direct interface in qd coordinates); (b) AVM VSI – Simscape Electrical built-in qd IM (Indirect interface in abc phase coordinates with snubbers); (c) AVM VSI – DCPVBR IM model (efficient interface in abc phase coordinates without snubbers).

The fourth model is established using the AVMs of VSI interfaced with the SE built-in qd IM model interfaced in abc coordinates. This type of interface requires both a one-time step delay and shunt resistive snubbers. Therefore, snubbers of 785Ω are added to the qd model, as illustrated in Figure 2.5(b), to limit the solution error to 2%.

The fifth proposed model is established using the AVMs of VSI interfaced using controlled voltages/current sources in abc coordinates with the DCPVBR IM model in abc coordinates and utilizes a one-time step delay block. This proposed model does not require artificial snubbers due to the VBR machine-network interface.

2.2 Computer Studies

To evaluate the numerical accuracy and computational performance of the subject machine-converter models, a typical VFD system depicted in Figure 2.1 is considered, with parameters summarized in Appendix A. The IM is assumed to supply mechanical power to the compressor coupled to its shaft with its torque-speed characteristics and inertia, also provided in Appendix A. For comparison, all the subject models, namely (1) Detailed VSI–SE built-in qd IM, (2) Detailed VSI–DCPVBR IM, (3) DI-AVM VSI– qd IM (direct interface in qd coordinates), (4) AVM VSI–SE built-in qd IM, and (5) AVM VSI–DCPVBR IM have been implemented using fixed time-step *ode4* solver in Offline PC simulation study using MATLAB/Simulink and Real-time OPAL-RT 5700 simulator using setup shown in Figure 2.6. The offline PC simulation studies have been simulated on PC Intel® Core™ i7-10750H and 3GHz processor.

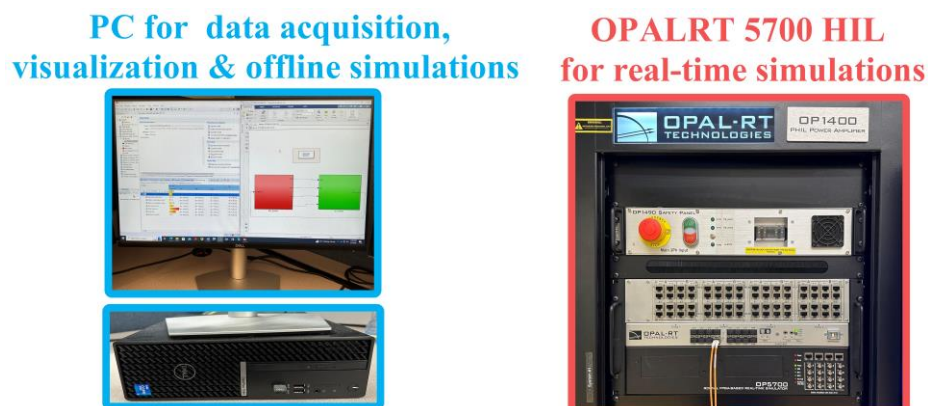


Figure 2.6 Implementation of subject models in offline and OPALRT5700 HIL real-time simulators using Simulink/RTLAB software.

2.2.1 Transient Study

For the V/Hz transient control study, it is considered that the system is starting from stall under speed command of 100 rad/s through a slew-rate limiter (SRL) with a slope of 60 rad/s, thus resulting in acceleration and inrush current and finally achieving the rotor mechanical speed of 100 rad/s within in 1.8s, as illustrated in Figure 2.7. At $t = 3$ s, a change in command speed from 100 rad/s to 200 rad/s is applied through a SRL with a slope of 60 rad/s. As a result, the transient current is reduced significantly, and the controller tracks the command speed. At $t = 4.8$ s, the desired 200 rad/s mechanical speed is achieved. Similar studies may be run multiple times to sweep a wide range of controller parameters, and therefore execution time is essential.

The response of phase voltage, current, torque, and speed obtained by the subject models simulated with a time step of 5 μ s are illustrated in Figure 2.7. As observed in Figure 2.7, all models produce consistent and accurate solutions, thus validating models that use AVM of VSC to accurately predict the average and fundamental components of the detailed switching model.

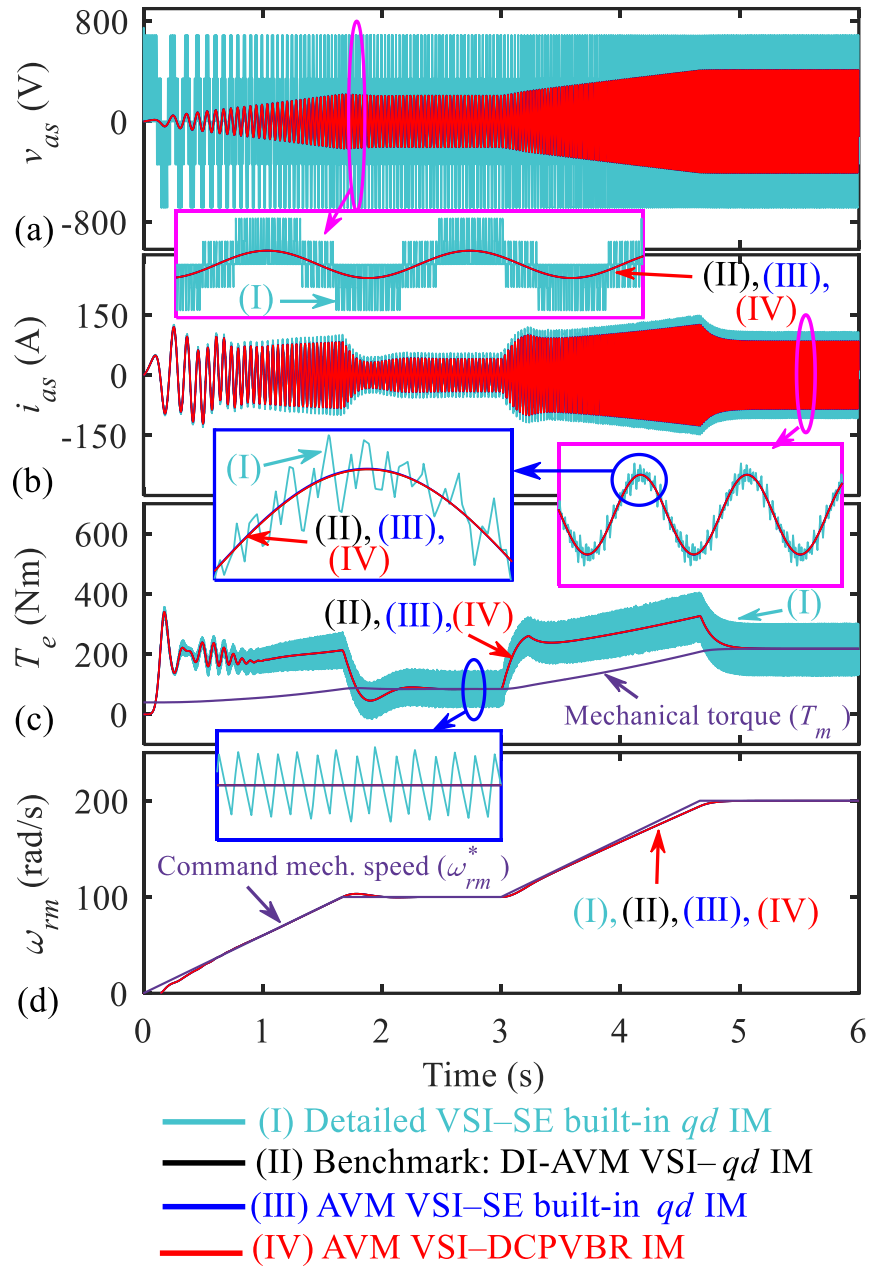


Figure 2.7 Transient response of system variables as produced by the subject models with $\Delta t = 5 \mu s$: (a) v_{as} , (b) i_{as} , (c) T_e , and (d) ω_{rm} .

2.2.2 Solution Accuracy

Here, the accuracy comparison of subject models simulated with different time steps is demonstrated. For this purpose, the benchmark system model utilizing the directly interfaced AVM of VSI with qd IM model (DI-AVM VSI- qd IM) is simulated with the small time-step of $1\mu\text{s}$. However, the other two models, namely the AVM VSI-SE built-in qd IM model and AVM VSI-DCPVBR IM model, are simulated with a fixed time-step of $200\mu\text{s}$. The magnified plots of these models are illustrated in Figure 2.8.

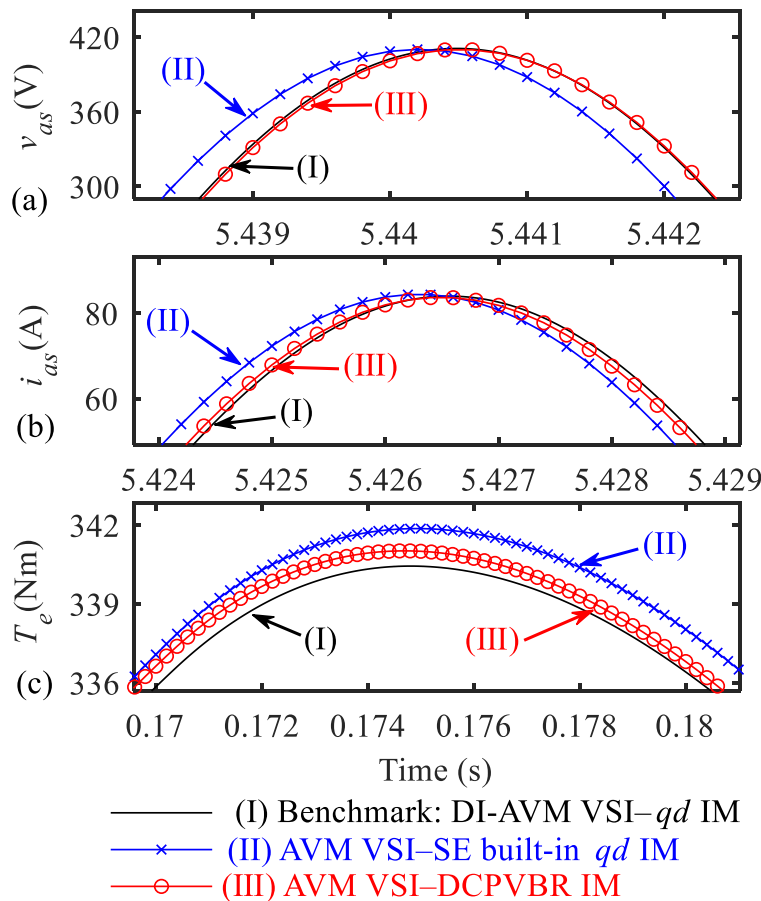


Figure 2.8 Magnified view of several variables from Figure 2.7, as obtained by the subject models with $\Delta t = 200\mu\text{s}$: (a) v_{as} , (b) i_{as} , and (c) T_e .

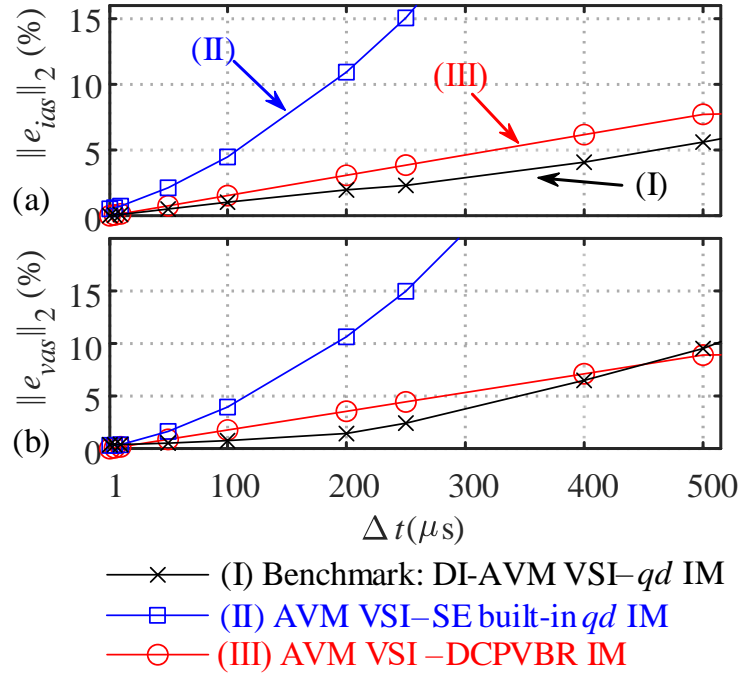


Figure 2.9 2-norm error of the subject models over 6 s transient case study with several different time-step sizes:(a) 2-norm phase “a” current error, (b) 2-norm phase “a” voltage error.

It is observed that the AVM VSI-SE built-in qd IM model produces inaccurate solution results at 200 μs due to its interface that uses artificial snubbers and a one-time step delay in the AVM of VSI. Despite a one-time step delay in the interface of the AVM VSI-DCPVBR IM model, it still remains stable and produces accurate results even at larger time steps.

Figure 2.9 illustrates the 2-norm errors in phase a current, and voltage for different time steps. As seen in Figure 2.9, the accuracy of the AVM VSI-SE built-in qd IM model deteriorates at medium time steps, and its 2-norm error exceeds 5% when 100 μs time-step is used. However, the proposed AVM VSI-DCPVBR IM model yields superior results in terms of numerical accuracy with a large time-step size of 300 μs while achieving a 2-norm error below 5%. The benchmark (DI-AVM VSI- qd IM) model yields the best performance in terms of numerical

accuracy with a large time-step size of $350\mu\text{s}$ while having a 2-norm error below 5%. Therefore, it is deduced that AVM VSI-SE built-in qd IM model produces a large error and cannot be simulated at large time steps. Meanwhile, the DI-AVM VSI- qd IM (benchmark) and AVM VSI-DCPVBR IM (proposed) models permit simulations with larger time steps while maintaining reasonable numerical accuracy.

2.2.3 Computational Performance

The computational performance of the subject models simulated offline and in the real-time simulator with the *ode4* fixed time-step solver is summarized in Table 2.1.

Table 2.1 Offline and real-time simulation performance comparisons of the subject models for the 6-second transient study with *ode4* solver

System Model	Max. possible time-step	Time-step size (Δt) (μs)	Steps	CPU time per step (μs)	CPU time (s)	OP5700 CPU Usage
Detailed VSI-SE built-in qd IM	$\sim 10\mu\text{s}$	5	12×10^5	29.36	35.23	29.61 %
		50	12×10^4	31.58	3.79	3.19 %
		300	not valid	not valid	not valid	not valid
Detailed VSI-DCPVBR IM	$\sim 10\mu\text{s}$	5	12×10^5	21.48	25.77	28.65 %
		50	12×10^4	24.31	2.92	3.16 %
		300	not valid	not valid	not valid	not valid
DI-AVM VSI- qd IM (direct interface in qd coordinates)	$\sim 350\mu\text{s}$	5	12×10^5	15.03	18.04	21.88 %
		50	12×10^4	17.33	2.08	2.27 %
		300	2×10^4	24.5	0.49	0.4 %
AVM VSI-SE built-in qd IM	$\sim 100\mu\text{s}$	5	12×10^5	30.49	36.59	32.96 %
		50	12×10^4	32.5	3.90	3.34 %
		300	not valid	not valid	not valid	not valid
AVM VSI-DCPVBR IM	$\sim 300\mu\text{s}$	5	12×10^5	21.71	26.05	31.62 %
		50	12×10^4	25.08	3.01	3.31 %
		300	2×10^4	33.9	0.68	0.56 %

As observed from offline simulation results in Table 2.1, the detailed switching models, namely as detailed VSI–SE built-in *qd* IM and detailed VSI–DCPVBR IM models due to their discrete switching events and zero-crossing detection requirements, cannot be simulated with a large time-step size $300\mu\text{s}$ thus remain invalid at larger time steps. However, the detailed VSI–DCPVBR IM model, due to DCPVBR’s direct machine-switching network interface and lower stiffness ratio, works ~ 1.36 times faster in offline simulation than the detailed VSI–SE built-in *qd* IM with 785Ω snubbers in addition to the snubbers inside VSI’s transistor switches in terms of lower total CPU time (25.77s vs 35.23s run with $5\mu\text{s}$ and 2.92s vs 3.79s run with $50\mu\text{s}$) and larger average CPU time-step size ($21.48\mu\text{s}$ vs $29.36\mu\text{s}$ run with $5\mu\text{s}$ and $24.31\mu\text{s}$ vs $31.58\mu\text{s}$ run with $50\mu\text{s}$). The AVM VSI–SE built-in *qd* IM model, although it avoids discrete switching events but requires 785Ω snubbers for *qd* indirect machine-switching network interface and one time-step delay of AVM VSI. As a result, the AVM VSI–SE built-in *qd* IM model takes (36.59s run with $5\mu\text{s}$, and 3.90s run with $50\mu\text{s}$) total CPU time and ($30.49\mu\text{s}$ run with $5\mu\text{s}$ and $32.5\mu\text{s}$ run with $50\mu\text{s}$) average CPU time-step size and also, it cannot be simulated with large time-step size $300\mu\text{s}$ thus remain invalid at larger time-step sizes. On the other hand, both the benchmark DI-AVM VSI–*qd* IM and the proposed AVM VSI–DCPVBR IM (with one time-step delay in VSI AVM but possess direct and efficient machine-switching network interface) models yield significant computational advantages in terms of permitting simulations with much larger time-step of $300\mu\text{s}$, which is very useful for system-level studies with larger time-steps. As seen in Table 2.1, the benchmark and proposed models consume a total CPU time of (18.04s and 26.05s vs 35.23s , 25.77s , and 36.59s run with $5\mu\text{s}$; 2.08s and 3.01s vs 3.79s , 2.92s and 3.9s run with $50\mu\text{s}$; 0.49s and 0.68s vs invalid solution results of other subject models run with $300\mu\text{s}$).

As seen from real-time simulation results of the subject models executed on OPALRT-5700 simulator in Table 2.1, the OP5700 CPU usage of detailed VSI–DCPVBR IM model and detailed VSI–SE built-in *qd* IM are (28.65% vs 29.61% run with 5 μ s and 3.16% vs 3.19% run with 50 μ s) and maximum permissible time-step of 10 μ s to avoid zero-crossing detection error and invalid results. However, the OP5700 CPU usage of AVM VSI–SE built-in *qd* IM model is comparable with detailed switching VSC-based models due to *qd* IM model’s snubbers (i.e. 32.96% vs 28.65% and 29.61% run with 5 μ s; 3.34% vs 3.16% vs 3.19% run with 50 μ s) and still it can be simulated with time-step of 100 μ s as opposed to detailed switching VSC-based models. Contrarily, both the benchmark DI-AVM VSI–*qd* IM and the proposed AVM VSI–DCPVBR IM model yield superior computational performance in terms of real-time simulation with time-step magnitude order of approximately ~300-350 μ s while maintaining acceptable accuracy. As seen from Table 2.1, the OP5700 CPU usage of these both models are 21.88% and 31.62% vs 32.96%, 28.65%, and 29.61% run with 5 μ s; 2.27% and 3.31% vs 3.34%, 3.16% vs 3.19% run with 50 μ s; 0.4% and 0.56% vs invalid solution results of other subject models run with 300 μ s). The snapshot depicting the %CPU utilization of the proposed AVM VSI–DCPVBR IM model executed on OPALRT 5700 simulator with 300 μ s is also shown in Figure 2.10.

Probes	Info				Data
	Usage [%]	Min	Max	Mean	1
Indirect_DCPVBR...SI Ts=3.0E-4[s]	0.56%				
SM_System Ts...142492354E-4[s]	0.56%	dt= 1.63 [us]	dt= 1.78 [us]	dt= 1.69 [us]	dt= 1.71 [us]
New data acquisition	0.01%	dt= 0.02 [us]	dt= 0.05 [us]	dt= 0.02 [us]	dt= 0.02 [us]
Major computation time	0.12%	dt= 0.36 [us]	dt= 0.40 [us]	dt= 0.37 [us]	dt= 0.37 [us]
Minor computation time	0.27%	dt= 0.79 [us]	dt= 0.83 [us]	dt= 0.80 [us]	dt= 0.80 [us]
Execution cycle	0.56%	dt= 1.63 [us]	dt= 1.78 [us]	dt= 1.69 [us]	dt= 1.71 [us]
Total step size	100.0%	dt= 299.99 [us]	dt= 300.01 [us]	dt= 300.00 [us]	dt= 300.00 [us]
Total idle	99.31%	dt= 296.36 [us]	dt= 298.09 [us]	dt= 297.92 [us]	dt= 297.97 [us]
Update lv panels	0.0%	dt= 0.00 [us]	dt= 0.00 [us]	dt= 0.00 [us]	dt= 0.00 [us]

Figure 2.10 Snapshot depicting the percentage CPU utilization of proposed VSI–DCPVBR IM model executed on OPALRT 5700 simulator with 300 μ s.

Finally, it is concluded that the benchmark DI-AVM VSI–*qd* IM model and the proposed AVM VSI–DCPVBR IM model are both computationally more efficient than the other models in both offline and real-time simulations when simulated with several different time-step sizes. It is concluded that the proposed AVM VSI–DCPVBR IM model yields good simulation performance and numerical accuracy while permitting relatively large time steps, which is desirable for system-level studies.

Chapter 3: Reconfigurable Star-Delta VBR Induction Machine Model for Predicting Soft-Starting Transients

Induction machines (IMs), due to their robustness, reliability, low cost, simple design, and self-starting capability, are extensively utilized in many commercial and industrial applications [2]–[5]. Simulations of such machines to analyze their starting and operational performance require numerically accurate and efficient models. The conventional qd model [17], although simple to implement, requires snubber circuits for interfacing with an external network, which reduces the accuracy and makes the model computationally expensive [49].

Traditionally, in EMT simulation programs, IMs are modelled using $qd0$ equivalent circuit [17]. In the classical $qd0$ model, both stator and rotor variables are transformed into qd coordinates, thus resulting in decoupled and rotor position-independent inductances. However, the indirect interface of the $qd0$ model with external inductive or switching circuits using resistive or capacitive snubber circuits enforces additional numerical error in the solution and leads to numerical stiffness and simulation inefficiency [49].

To overcome the limitations of qd model, the CP-VBR formulations of the induction machine model; namely VBR–I, II, III models, have been proposed in [18]. The VBR formulations represent the stator interfacing circuit in abc phase coordinates as three-phase controlled voltage sources behind three-phase RL branches and the rotor subsystem in qd coordinates with rotor flux linkages as state-variables. As a result, the VBR models become non-stiff, numerically accurate, and efficient because they enable direct interconnection of the stator interfacing circuit with arbitrary inductive or power-electronic circuits without snubbers, thus making them useful for

power system simulation studies. According to [18], the VBR–I and VBR–II models are suitable to represent both wye/star (Y) and delta (Δ) machine stator winding configurations. The VBR–III model has decoupled RL branches and is suitable to represent the wye (Y) machine stator winding configuration only.

To employ the advantageous properties of the CPVBR models, it can be preferable to switch between the star- and delta-connected stator windings under different conditions of starting and operational performance of the induction motor. Therefore, this chapter extends the prior work and presents a reconfigurable star-delta constant-parameter voltage-behind-reactance (CPVBR) model of a three-phase squirrel-cage IM considering the low-frequency deep-rotor-bar phenomenon. The eigenvalue analysis and computer studies demonstrate that the proposed model yields superior computational performance while providing an efficient machine-network interface as compared to the established qd model. It is envisioned that the new model can be useful for the efficient simulation of power systems, including induction machines with star-delta starters.

3.1 VBR Formulation with Variable Rotor Resistance

Herein, a three-phase squirrel-cage IM with either wye (Y)-connected or delta(Δ)-connected stator windings is assumed. For simplicity, magnetic saturation is not considered. All rotor parameters are referred to the stator side, and motor sign convention is used. The CPVBR formulations of the induction machine proposed in [18] are based on the classical $qd0$ equivalent circuit model [17] in an arbitrary reference frame, as shown in Figure 3.1. The interested reader can find a more detailed derivation of the CPVBR models in [18].

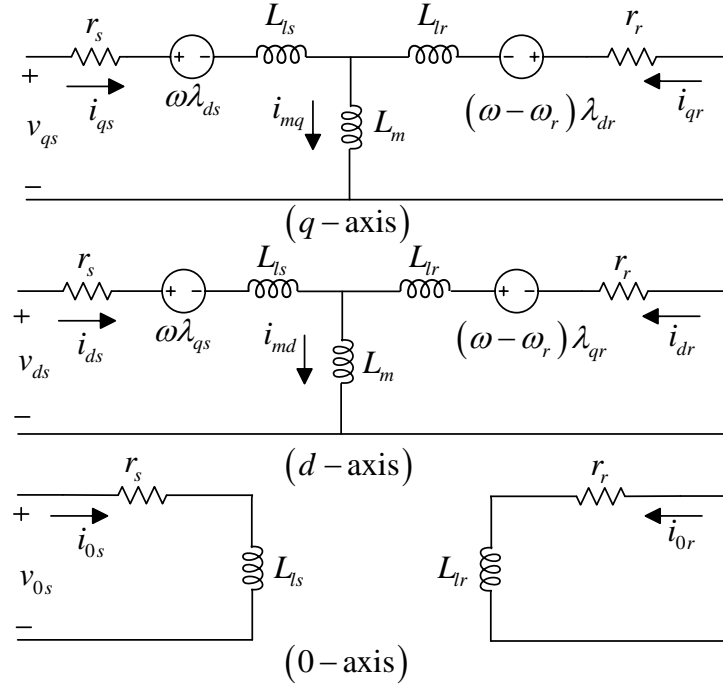


Figure 3.1 Classical $qd0$ equivalent circuit in arbitrary reference frame for a three-phase squirrel-cage induction machine.

It is important to note that during the starting electromechanical transients, the rotor resistance may change significantly with the changes in slip and frequency of the rotor currents due to the deep-rotor-bar effect in the squirrel-cage rotor structure. To account for this effect, the single equivalent rotor resistance can be made speed-dependent using a simple linear approximation method proposed in [50]. According to [50], the speed-dependent rotor resistance can be written as

$$r_r(\omega_r) = r_{r1} + s(r_{r2} - r_{r1}), \quad (3.1)$$

where, r_{r1} and r_{r2} correspond to low-slip ($s \approx 0$) and stand-still ($s \approx 1$) rotor resistance values, respectively. The slip s is expressed as

$$s = \frac{n_s - n_r}{n_s} = \frac{\omega_s - \omega_r}{\omega_s}. \quad (3.2)$$

Herein, the CP-VBR-II model [18] is considered as it remains valid for both Y- and Δ -stator windings connections. To better predict the low-frequency deep-rotor-bar phenomenon, the CP-VBR-II model is modified by assuming the speed-dependent variable rotor resistance $r_r(\omega_r)$ in the model equations. Based on the $qd0$ model equivalent circuit of Figure 3.1 and considering the low-frequency deep-rotor-bar effect, the rotor flux linkages λ_{qdr} chosen as the state variables can be expressed as

$$p\lambda_{qr} = -r_r(\omega_r)i_{qr} - (\omega - \omega_r)\lambda_{dr}, \quad (3.3)$$

$$p\lambda_{dr} = -r_r(\omega_r)i_{dr} + (\omega - \omega_r)\lambda_{qr}. \quad (3.4)$$

where p is the Heaviside's derivative operator d/dt , $r_r(\omega_r)$ is the variable rotor resistance as a function of rotor speed, ω is the electrical angular frequency of the arbitrary reference frame, and ω_r is the electrical angular frequency of the rotor. The rotor currents can be expressed in terms of rotor flux linkages and magnetizing flux linkages as [17]

$$i_{qr} = \frac{1}{L_{lr}}(\lambda_{qr} - \lambda_{mq}), \quad (3.5)$$

$$i_{dr} = \frac{1}{L_{lr}}(\lambda_{dr} - \lambda_{md}). \quad (3.6)$$

where L_{lr} denotes rotor leakage inductance. Replacing the rotor currents from (3.5)–(3.6) in (3.3)–(3.4), the final rotor state equation becomes

$$p\lambda_{qr} = -\frac{r_r(\omega_r)}{L_{lr}}(\lambda_{qr} - \lambda_{mq}) - (\omega - \omega_r)\lambda_{dr}, \quad (3.7)$$

$$p\lambda_{dr} = -\frac{r_r(\omega_r)}{L_{lr}}(\lambda_{dr} - \lambda_{md}) + (\omega - \omega_r)\lambda_{qr}. \quad (3.8)$$

In (3.7)–(3.8), the q - and d -axes mutual flux linkages are

$$\lambda_{mq} = L_m'' \left(i_{qs} + \frac{\lambda_{qr}}{L_{lr}} \right), \quad (3.9)$$

$$\lambda_{md} = L_m'' \left(i_{ds} + \frac{\lambda_{dr}}{L_{lr}} \right). \quad (3.10)$$

where L_m'' is defined as [18]

$$L_m'' = (L_m^{-1} + L_{lr}^{-1})^{-1}. \quad (3.11)$$

The stator flux linkages can be written in terms of stator currents and rotor flux linkages as

$$\lambda_{qs} = (L_{ls} + L_m'')i_{qs} + \frac{L_m''}{L_{lr}}\lambda_{qr}, \quad (3.12)$$

$$\lambda_{ds} = (L_{ls} + L_m'')i_{ds} + \frac{L_m''}{L_{lr}}\lambda_{dr}, \quad (3.13)$$

$$\lambda_{0s} = L_{ls}i_{0s}. \quad (3.14)$$

where L_{ls} denotes stator leakage inductance. Substituting the stator flux linkages from (3.12)–(3.14) into stator voltages equations in [18] gives,

$$\begin{bmatrix} v_{qs} \\ v_{ds} \\ v_{0s} \end{bmatrix} = r_s \begin{bmatrix} i_{qs} \\ i_{ds} \\ i_{0s} \end{bmatrix} + \mathbf{L}_{qd0}'' p \begin{bmatrix} i_{qs} \\ i_{ds} \\ i_{0s} \end{bmatrix} + \begin{bmatrix} \omega(L_{ls} + L_m'')i_{ds} \\ -\omega(L_{ls} + L_m'')i_{qs} \\ 0 \end{bmatrix} + \begin{bmatrix} e_q'' \\ e_d'' \\ 0 \end{bmatrix}. \quad (3.15)$$

where \mathbf{L}_{qd0}'' is defined as

$$\mathbf{L}_{qd0}'' = \begin{bmatrix} L_{ls} + L_m'' & 0 & 0 \\ 0 & L_{ls} + L_m'' & 0 \\ 0 & 0 & L_{ls} \end{bmatrix}. \quad (3.16)$$

In the CPVBR-II model, the sub-transient back-emf voltages in q - and d - axes are calculated as

$$e_{qs}'' = \frac{\omega_r L_m''}{L_{lr}} \lambda_{dr} + \frac{L_m'' r_r(\omega_r)}{L_{lr}^2} \left(\frac{L_m''}{L_{lr}} - 1 \right) \lambda_{qr} + \frac{L_m''^2 r_r(\omega_r)}{L_{lr}^2} i_{qs}, \quad (3.17)$$

$$e_{ds}'' = \frac{-\omega_r L_m''}{L_{lr}} \lambda_{qr} + \frac{L_m'' r_r(\omega_r)}{L_{lr}^2} \left(\frac{L_m''}{L_{lr}} - 1 \right) \lambda_{dr} + \frac{L_m''^2 r_r(\omega_r)}{L_{lr}^2} i_{ds}, \quad (3.18)$$

Transformation of (3.15) into abc phase coordinates by applying the inverse Park transformation matrix $\mathbf{K}_s^{-1}(\theta)$ gives the constant-parameter stator interfacing circuit model as follows

$$\mathbf{v}_{abc} = r_s \mathbf{i}_{abc} + \mathbf{L}_{abc}'' p \mathbf{i}_{abc} + \mathbf{e}_{abc}'', \quad (3.19)$$

where the transformed sub-transient back-emf voltage sources in abc coordinates are defined as

$$\mathbf{e}_{abc}'' = \mathbf{K}_s^{-1}(\theta) \begin{bmatrix} e_{qs}'' & e_{ds}'' & 0 \end{bmatrix}^T. \quad (3.20)$$

In (3.19), the constant-parameter inductance matrix \mathbf{L}_{abc}'' of the stator interfacing circuit is calculated as

$$\mathbf{L}_{abc}'' = \mathbf{K}_s^{-1}(\theta) \mathbf{L}_{qd0s}'' \mathbf{K}_s(\theta) = \begin{bmatrix} L_S & L_M & L_M \\ L_M & L_S & L_M \\ L_M & L_M & L_S \end{bmatrix}, \quad (3.21)$$

In (3.21), the self- and mutual- inductances of the stator interfacing circuit are defined as

$$L_S = L_{ls} + \frac{2}{3} L_m'', \quad (3.22)$$

$$L_M = -\frac{1}{3}L_m'' \quad (3.23)$$

The electromagnetic torque and electrical rotor speed equations can also be written as [18]

$$T_e = \left(\frac{3P}{4} \right) (\lambda_{md} i_{qs} - \lambda_{mq} i_{ds}), \quad (3.24)$$

$$p\omega_r = \frac{P}{2J} (T_e - T_m). \quad (3.25)$$

Finally, the CPVBR–II model [18] with the inclusion of low-frequency deep-rotor-bar effects constitutes a rotor state-space model (3.7)–(3.10), (3.17)–(3.18), stator interfacing circuit (3.19), and mechanical subsystem (3.24)–(3.25). The implementation of the CPVBR–II model and its interfacing circuit for both Y- and Δ - connected stator windings is shown in Figure 3.2, where three-phase controlled voltage sources behind three-phase RL branches representing stator interfacing circuit are used to enable its direct interface with an arbitrary external network without shunt snubbers. The stator currents in CPVBR–II model are selected as inputs to the rotor and mechanical subsystem to calculate the sub-transient back-emf voltages in abc coordinates, as inputs to controlled voltage sources. This model utilizes two three-phase switches, “1, 2” to reconfigure the machine stator windings connections into either Y or Δ in the run-time. For example, closing of the three-phase switch “2” connects the stator winding terminals (a' , b' , c') to terminal points (2), consequently resulting in a Y-connected IM configuration and vice versa.

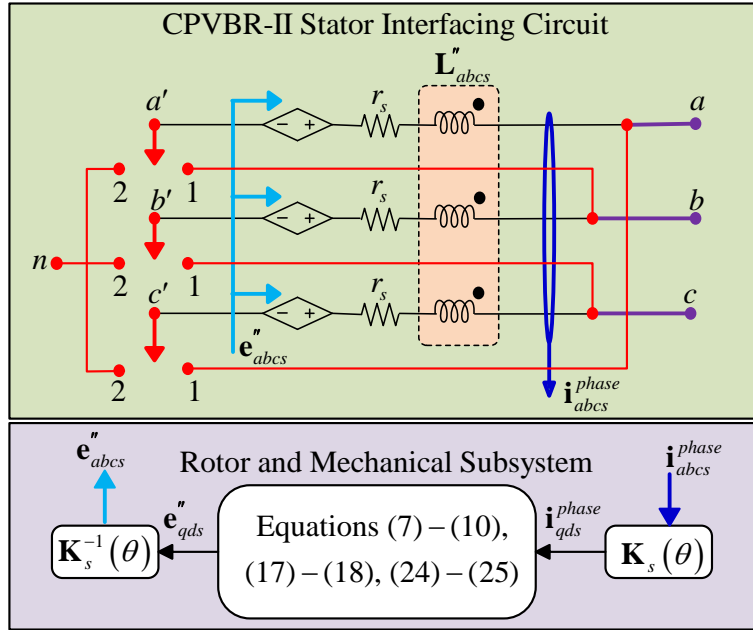


Figure 3.2 Implementation of CPVBR-II model of a three-phase squirrel-cage induction machine for reconfigurable wye- and delta-connected stator windings.

3.2 Simulation Studies

To validate the simulation results and numerical performance of the considered models, a simple case system depicted in Figure 3.3 is considered. Herein, a 460V 50hp squirrel-cage IM with either wye- or delta-connected stator windings, is connected to the power grid (represented by ideal voltage sources e_{abc}) through power cables (represented by r_{line} and L_{line}). The system parameters are summarized in Appendix B.

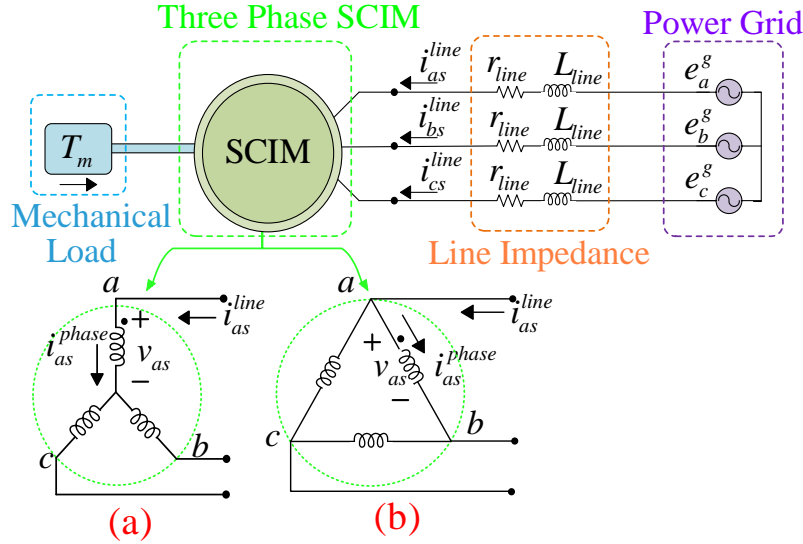


Figure 3.3 The test system consisting of a three-phase squirrel-cage induction machine connected to a power grid through power cables: (a) wye-connected machine, and (b) delta-connected machine.

For the purpose of accuracy and efficiency comparison, both the classical qd and the proposed reconfigurable Y- Δ CPVBR models considering the deep-rotor-bar phenomenon, have been implemented and simulated in MATLAB-Simulink software. The models were solved using *ode3* fixed time-step solver (with different time-steps), and also *ode45* and *ode23tb* variable time-step solvers (with absolute and relative tolerances set to 10^{-4}). The synchronous reference frame is used in all subject models. Due to the qd model's indirect interface with external inductive or switching circuits, the shunt resistive snubbers of 982Ω (corresponding to 100pu) are considered to limit the solution error to 1% for the qd model. The interfacing circuit of qd model for both Y- and Δ -connected stator windings is shown in Figure 3.4, where three-phase controlled current sources connected in parallel with snubber resistors are used to obtain its compatible interface with external inductive or switching power networks. For consistency, all simulations have been run on a PC with Intel[®] Core[™] i7-10750H @ 3GHz processor.

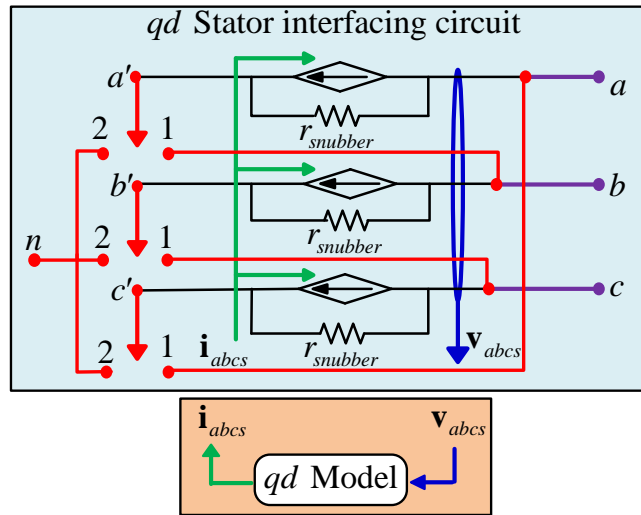


Figure 3.4 Implementation of qd model of a three-phase squirrel-cage induction machine for wye-connected and delta-connected stator windings.

3.2.1 DOL Starting of Delta-connected Motor

In this study, the squirrel-cage IM with Δ -connected stator windings is assumed to start from zero initial conditions under nominal operating voltages. The configuration of this study is shown in Figure 3.3(b). A no-load start-up transient study followed by a load torque change is simulated for 4 s. At $t = 2$ s, the step change in load torque from zero to 198 Nm is applied to the machine, and the simulation is run until 4 s. Figure 3.5 presents the transient responses of several variables obtained by the subject models. As can be observed in Figure 3.5, the CPVBR-II model and the qd model are consistent, and both accurately predict the system's transient and steady-state response. Also, for better clarity and comparison purposes, the magnified plots of selected variables from Figure 3.5 are depicted in Figure 3.6.

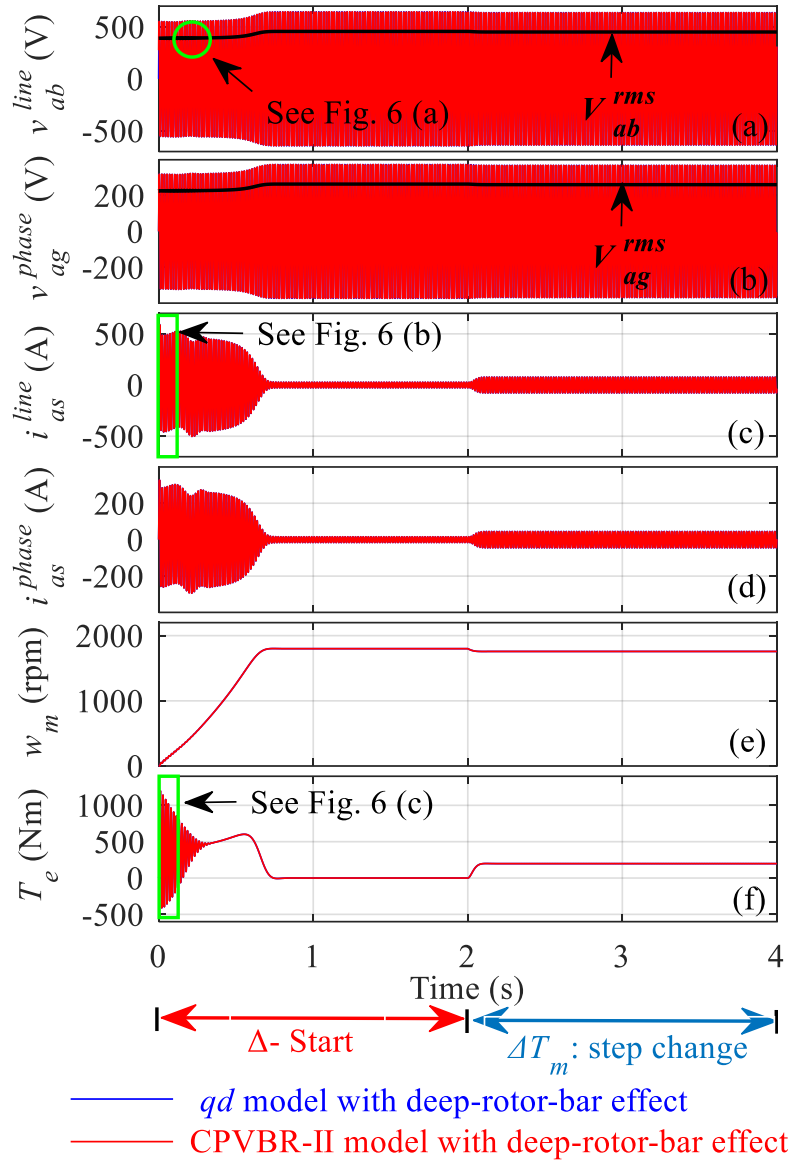


Figure 3.5 Transient response of system variables of Δ -connected IM as obtained by the subject models during start-up followed by a load change: (a) $v_{ab,line}$, (b) $v_{ag,phase}$, (c) $i_{as,line}$, (d) $i_{as,phase}$, (e) w_m , and (f) T_e .

In this considered study, the machine's stator windings are energized from a three-phase voltage source with a phase-phase voltage of 460V, so the rotor of the machine begins to accelerate from a standstill to reach a steady-state speed. As observed in Figures 3.5–3.6, the starting inrush

current and torque pulsations are significant, which consequently causes voltage dip across the machine terminals. During the start-up, the voltage dip level reaches about 15%, and it recovers approximately at $t = 0.8$ s when the motor reaches a steady-state. Then, as a result of a step-change in load torque at $t = 2$ s, the machine establishes a new operating condition, as illustrated in Figure 3.5.

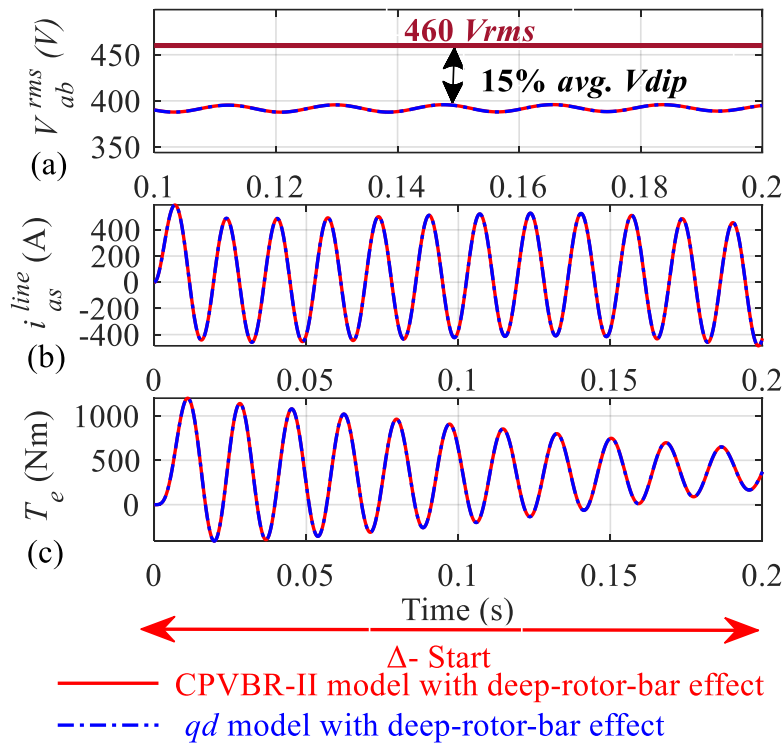


Figure 3.6 Magnified plots of selected variables during start-up of Δ -connected IM: (a) RMS line voltage $v_{ab,rms}$, (b) line current $i_{as,line}$, and (c) electromagnetic torque T_e .

Finally, it is deduced from the simulation results that starting squirrel-cage IMs in delta-connected stator windings will give poor starting performance in terms of high starting inrush

currents, increased voltage dips, and increased stresses on power utility equipment during their start-up, which may lead to power system instability.

It is worth mentioning that the new CPVBR–II model with low-frequency deep-rotor-bar-effect has been verified against the qd model with the low-frequency rotor-bar-effect. The inclusion of the deep-bar-rotor effect in the subject models produces more accurate simulation results during starting transient and steady-state periods, as has been demonstrated in [50]. At the same time, the models without deep-rotor-bar effects will consequently result in incorrect estimation of stator-currents and steady-state speed [50].

3.2.2 Wye/Delta Starting of SCIM

This study demonstrates the wye (Y) - delta (Δ) starting of the squirrel-cage IM. This method allows the motor to operate in Y-configuration, as shown in Figure 3.3(a), at reduced operating voltages (generally by $1/\sqrt{3}$). This leads to reduced power and inrush currents during start-up. Then, after some time, the motor is switched into Δ -configuration. A no-load start-up transient study followed by Y- Δ switching and load torque step change is simulated for 4 s. At $t = 2$ s, the stator winding configuration is switched from wye- to delta-connection resulting in switching transients. Then, at $t = 3$ s, a step-change in load torque from zero to 198 Nm is applied to the machine and continued to run until 4 s. The transient responses of selected variables obtained by the subject models are demonstrated in Figure 3.7. For comparison purposes, the magnified views of selected variables from Figure 3.7 are also shown in Figure 3.8.

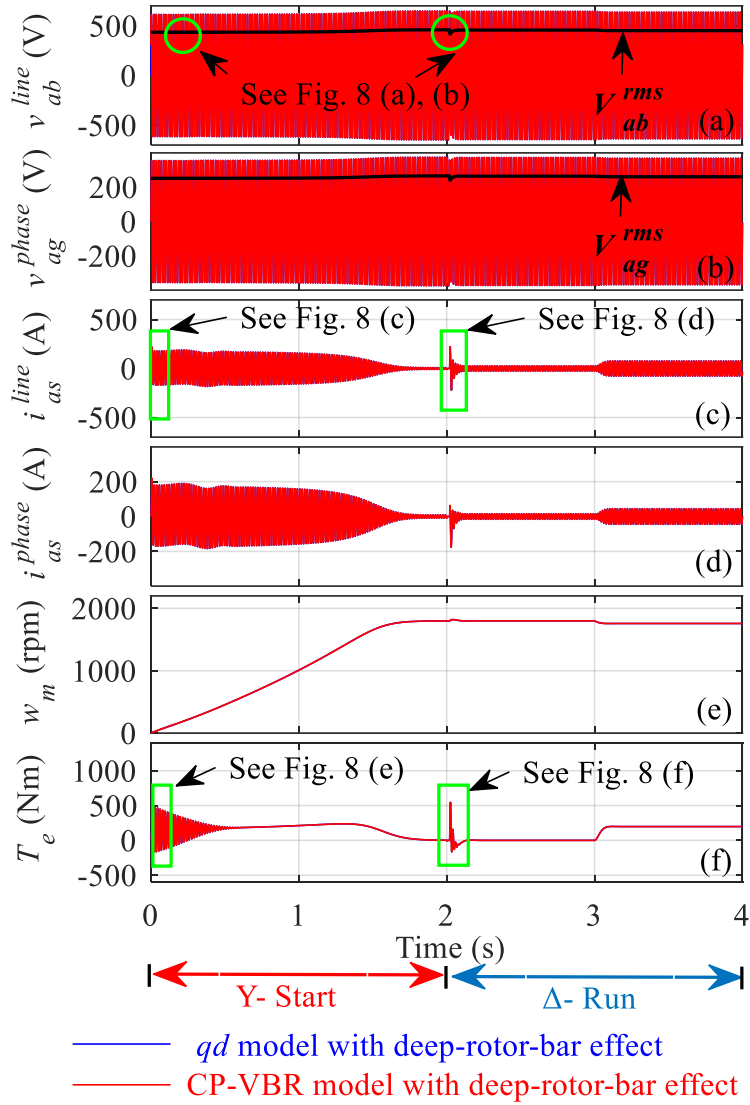


Figure 3.7 Transient response of system variables of Y-Δ starter-based IM as obtained by the subject models during start-up followed by Y-Δ switching and load change: (a) $v_{ab, line}$, (b) $v_{ag, phase}$, (c) $i_{as, line}$, (d) $i_{as, phase}$, (e) w_m , and (f) T_e .

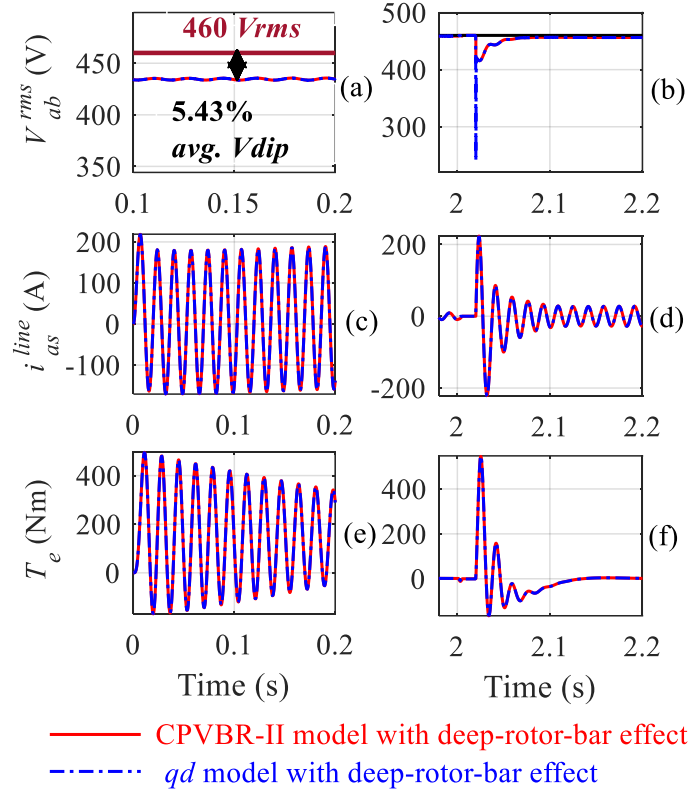


Figure 3.8 Magnified views of selected variables under: (a), (c), and (e) wye-connected IM starting condition; and (b), (d), and (f) Y- Δ switching transition.

During this study, the machine's stator phase windings are initially energized from a voltage of $460/\sqrt{3}$ V, due to which the motor starts to accelerate from a standstill to a steady state. As observed from Figures 3.7–3.8, the machine draws lower starting inrush currents, produces lower torque pulsations, and has a slower dynamic response as compared to the delta-connected study in Figures 3.5–3.6. This happens due to a reduction in operating voltages across the stator phase winding terminals. Consequently, it improves the motor starting by reducing starting inrush currents flowing through stator windings and also reducing the voltage dips across the machine

terminals. For our case, the voltage dip is now reduced to about 5.43%, which is in the appropriate range. This voltage dip is cleared after $t = 1.8$ s once the steady-state condition is reached.

After reaching the steady-state operating condition, the stator winding configuration is switched from Y to Δ causing switching transients in the system, which vanishes quickly. It is worth noting that this open transition star-delta switching causes voltage dips, current spikes, and torque surges, which sometimes may become much worse depending on the switching time and loading condition, consequently leading to failure of power system operation. Therefore, for safe operation, a small switchover transition delay of 20ms is introduced due to which star(Y)-connection switches open at $t = 2$ s and delta(Δ)-connection switches close at $t = 2.02$ s resulting in switching transients and voltage dip of 9.78% for CPVBR-II model which is within an acceptable range and cleared in very short time duration. Then, at $t = 3$ s, a load torque of 198 Nm is applied to the machine causing it to establish a new operating condition.

It is also seen in Figures 3.7–3.8 that the proposed CPVBR model and the qd model produced consistent results. However, the qd model produces a deviation in predicting voltage dips during Y- Δ switching transients which is due to interfacing error introduced by 1% of current flowing through the snubbers.

3.2.3 Computational Performance

Although the considered models produce consistent and matching simulation results, their computational properties are quite different. The computational performance of the subject models simulated using both fixed- (*ode3* solver) and variable-time-step solvers (non-stiff *ode45* and stiff *ode23tb* solvers) are summarized in Tables 3.1 and 3.2.

Table 3.1 Computational performance comparisons of the subject models for the 4-second wye-delta starting transient case study using non-stiff *ode45* and stiff *ode23tb* variable time-step solvers

Solver	Model	Largest eigenvalue	Steps	CPU time per step (μs)	CPU time (s)
<i>ode45</i>	<i>qd</i> model (snubber)	-3.9×10^6	3122687	84.6	264.2
<i>ode23tb</i>			38418	197.8	7.6
<i>ode45</i>	CPVBR-II model	$-6.4 \pm 377i$	13177	258	3.4
<i>ode23tb</i>			16543	211.6	3.5

Table 3.2 Computational performance comparisons of the subject models for the 4-second wye-delta starting transient case study using *ode3* fixed time-step solver

Model	Time step (Δt)	Largest eigenvalue	Steps	CPU time per step (μs)	CPU time (s)
<i>qd</i> model (with snubbers)	$1 \mu\text{s}$	-1.09×10^5	4×10^6	22.7	90.8
	$100 \mu\text{s}$	-2.44×10^3	–	–	cannot run
CPVBR-II model	$1 \mu\text{s}$	$-6.42 \pm 377i$	4×10^6	83.5	333.9
	$100 \mu\text{s}$	$-6.38 \pm 377i$	4×10^4	85.5	3.42

It is observed in Table 3.1, 3.2 that CPVBR possesses better-scaled eigenvalues and a lower stiffness ratio as compared to the *qd* model. As seen in Table 3.1 from results obtained using the non-stiff *ode45* solver, the CPVBR model is computationally more efficient than the *qd* model in terms of faster simulation speed (3.4 s vs 264.2 s), fewer steps (13177 vs 3122687) and larger average time-step size (258 μs vs 84.6 μs).

Since the *qd* model becomes numerically stiff due to shunt snubbers, it can be observed in Table 3.1 that when it is simulated with the stiff *ode23tb* solver, the computational burden is

reduced significantly by allowing smaller steps (38418) and CPU time (7.6 s) for the same 4 s transient study. However, the CPVBR model using *ode23tb* solver, still works faster than the *qd* model in terms of much smaller steps (16543 vs 38418) and CPU time (3.5 s vs 7.6 s) due to its lower numerical stiffness.

As observed in Table 3.2 from the results obtained using fixed time-step solver *ode3*, the *qd* model is only capable of producing results at smaller time steps. However, it yields a faster simulation speed (90.8s vs 333.9s) when run using fixed time-step solvers at a very small time-step as compared to the CPVBR model. The CPVBR model works slower due to the use of snubber resistances in the switches for both subject models for fixed-time step study. The CPVBR model still has the advantage of running with larger time steps using fixed time-step solvers. This is particularly advantageous for large-scale power system studies where it is desirable to run the simulation with larger time steps.

Finally, it is deduced that the proposed CPVBR model possesses excellent numerical properties and simulation performance while accurately predicting the waveforms for several variables. The *qd* model produces a deviation in simulation results due to interfacing error and small currents flowing through the snubbers leading to reduced efficiency and accuracy.

Chapter 4: Wide-Band Constant-Parameter Voltage-Behind-Reactance Model of Squirrel-Cage Induction Machines

Variable frequency drives (VFDs) are widely utilized in many commercial and industrial applications [11]–[14], wherein typically, a three-phase squirrel-cage induction machine (IM) is fed from an inverter through a cable. To design and tune such systems, it is essential to develop efficient, accurate and wide-band models of IMs for studying the motor-converter interactions and low-to-high frequency phenomena. Although several classes of IM models have been proposed in the literature, which can be classified into: 1) low-frequency (e.g. PD, qd , VBR) models [15]–[18]; and 2) high-frequency behavioural circuit models [7], [12], [21], [24]–[34]. These low-frequency models do not represent the machine impedance characteristics and conducted EMI effects in the mid-high frequency range (i.e., several kHz to 10 MHz). At the same time, some of the high-frequency models offer limited scope and capabilities in predicting mid-to-high-frequency phenomena. Additionally, these high-frequency models [12], [25]–[28] feature complex structures and complicated parameterization methods. Moreover, these models do not predict low-frequency electromagnetic transients and motor slip variations.

This chapter presents a wide-band model for the IMs that is valid in the frequency range from DC to ten MHz. The new model is obtained by incorporating the low-mid frequency voltage-behind-reactance model [18] with the universal high-frequency stator circuit model [7] as well as the bearing circuit model [39]. The performance of the proposed model is demonstrated using computer simulations and experimental results obtained from a typical 7.5hp induction motor connected to a drive system through a cable. The new model is demonstrated to accurately predict the common mode (CM) and differential mode (DM) impedances, reflected transient over-

voltages, CM currents, and bearing voltages, all representing an advantage over the conventional/existing IM models.

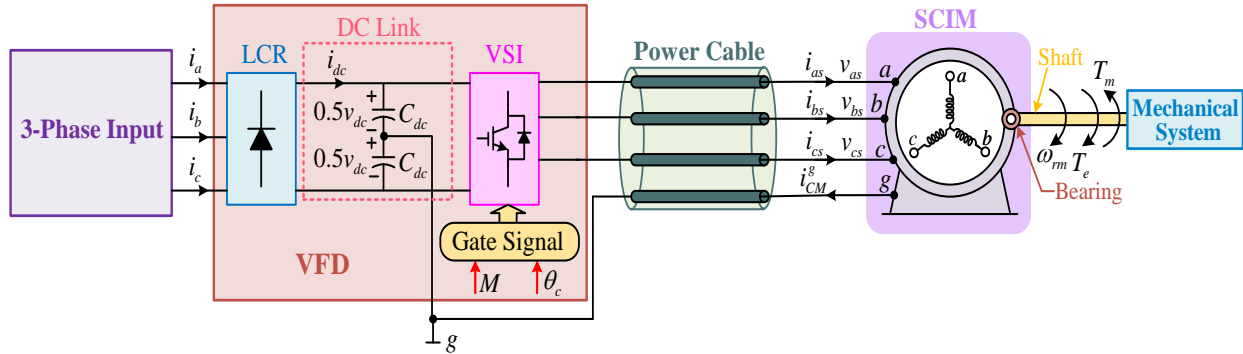


Figure 4.1 Typical three-phase VFD system consisting of a line-commutated rectifier (LCR) and a voltage-source-inverter (VSI), feeding a squirrel-cage induction motor (SCIM) through a power cable.

4.1 Modelling of Induction Machine

In this section, a typical VFD system as shown in Figure 4.1 is considered. Therein, a line-commutated rectifier (LCR) is used to produce a dc voltage from the three-phase power supply, which is then converted into variable frequency/amplitude three-phase ac voltages using a three-phase, two-level voltage-source inverter (VSI) to feed a squirrel-cage induction machine (SCIM) through a cable. The voltages across the upper and lower capacitors in the DC link are specified by $\pm 0.5v_{dc}$. The inputs to the VSI are the gate signals which are controlled by the modulation index M and converter angle θ_c , respectively. The IM is assumed to have Y-connected stator windings. The magnetic saturation is not considered since VFDs generally prevent over-saturation and may operate in a constant flux region (i.e., equivalent to Volts/Hz control). The mechanical system acting as the load is coupled to the shaft of IM. Additionally, the shaft of IM is linked with the stator frame through bearings, and the induced voltage across motor bearings is specified by v_B . The stator frame is connected to the middle point of the DC link through a cable lead, and the

current that flows out of the stator frame is specified as CM current (i_{CM}^g). The proposed WBDCPVBR IM model comprises three parts, i.e., the low-frequency sub-circuit and mechanical subsystem, the high-frequency stator sub-circuit, and the bearing circuit, which are explained subsequently. To simplify the notations, all variables are referred to the stator side.

4.1.1 Low-Frequency DCPVBR Model [18]

At lower frequencies (dc to ~10kHz), the IM behaviour is predominantly inductive, and the energy conversion is mainly realized through the air-gap flux, which is defined by the machine's stator and rotor currents. Therefore, the transient and steady-state behaviour of the induction machine may be well represented by the lumped-parameter low-frequency models. Specifically, the decoupled constant parameter voltage-behind-reactance (DCPVBR) [18] is selected to represent the Y-connected induction machine in the low-frequency range. This model possesses a constant-parameter direct interfacing with an arbitrary external network in SVB EMT simulation programs. For completeness, a summary of this model is briefly presented here.

In the DCPVBR model [18], the stator voltage equation considering zero-sequence is assumed to have the following form

$$\mathbf{v}_{abc s} = r_D \mathbf{i}_{abc s} + L_D p \mathbf{i}_{abc s} + \mathbf{e}_{abc s}'' + \underbrace{3r_0 i_{0s} + 3L_0 p i_{0s}}_{r_0 i_{ng} + L_0 p i_{ng}}, \quad (4.1)$$

where $\mathbf{v}_{abc s} = [v_{as} \ v_{bs} \ v_{cs}]^T$ represents the stator terminal voltages, $\mathbf{i}_{abc s} = [i_{as} \ i_{bs} \ i_{cs}]^T$ represents the stator currents, $\mathbf{e}_{abc s}'' = [e_{as}'' \ e_{bs}'' \ e_{cs}'']^T$ represents the so-called sub-transient back-emf voltages. The lower-case letter p denotes the Heaviside operator $p = d/dt$. The constant and

decoupled RL branch resistances and inductances (r_D and L_D) in addition to zero-sequence resistances and inductances (r_0 and L_0), are defined as

$$\left. \begin{aligned} r_D &= r_s + L_m''^2 L_{lr}^{-2} r_r, & L_D &= L_{ls} + L_m'', \\ r_0 &= -\frac{1}{3} L_m''^2 L_{lr}^{-2} r_r, & L_0 &= -\frac{1}{3} L_m''. \end{aligned} \right\} \quad (4.2)$$

Here, r_s and L_{ls} denote the original stator phase winding resistance and leakage inductance, respectively; r_r and L_{lr} denote the rotor winding resistance and leakage inductance, respectively.

Also, L_m'' is the sub-transient magnetizing inductance defined as [18]

$$L_m'' = \left(L_m^{-1} + L_{lr}^{-1} \right)^{-1}, \quad (4.3)$$

where L_m is the magnetizing inductance of the machine, In (4.1), \mathbf{e}_{abc}'' represents the transformed sub-transient back-emf voltages in abc coordinates and is obtained as

$$\mathbf{e}_{abc}'' = \begin{bmatrix} e_{as}'' & e_{bs}'' & e_{cs}'' \end{bmatrix}^T = \mathbf{K}_s^{-1}(\theta) \begin{bmatrix} e_{qs}'' & e_{ds}'' & e_{0s}'' \end{bmatrix}^T, \quad (4.4)$$

where $\mathbf{K}_s^{-1}(\theta)$ is the inverse Park's transformation matrix [17]. The q - and d - axes sub-transient back-emf voltages can be calculated as [18]

$$e_{qs}'' = \omega_r L_m'' L_{lr}^{-1} \lambda_{dr} + r_r L_m'' L_{lr}^{-2} \left(L_m'' L_{lr}^{-1} - 1 \right) \lambda_{qr}, \quad (4.5)$$

$$e_{ds}'' = -\omega_r L_m'' L_{lr}^{-1} \lambda_{qr} + r_r L_m'' L_{lr}^{-2} \left(L_m'' L_{lr}^{-1} - 1 \right) \lambda_{dr}. \quad (4.6)$$

The state-space equations of the rotor subsystem flux linkages in the qd coordinates can be expressed as

$$p \lambda_{qr} = r_r L_{lr}^{-1} \left(L_m'' L_{lr}^{-1} - 1 \right) \lambda_{qr} - (\omega - \omega_r) \lambda_{dr} + r_r L_{lr}^{-1} L_m'' i_{qs}, \quad (4.7)$$

$$p \lambda_{dr} = r_r L_{lr}^{-1} \left(L_m'' L_{lr}^{-1} - 1 \right) \lambda_{dr} + (\omega - \omega_r) \lambda_{qr} + r_r L_{lr}^{-1} L_m'' i_{ds}. \quad (4.8)$$

Here, ω is the arbitrary reference frame's electrical speed, and ω_r is the rotor's electrical speed, respectively. Also, i_{qs} and i_{ds} are the stator currents in qd coordinates, which are obtained as

$$\mathbf{i}_{qds} = \begin{bmatrix} i_{qs} & i_{ds} & i_{0s} \end{bmatrix}^T = \mathbf{K}_s(\theta) \begin{bmatrix} i_{as} & i_{bs} & i_{cs} \end{bmatrix}^T. \quad (4.9)$$

Here, $\mathbf{K}_s(\theta)$ is Park's transformation matrix [17]. The electromagnetic torque and mechanical dynamics are expressed as

$$T_e = \left(\frac{3P}{4} \right) \left(\frac{L_m''}{L_r} \right) (\lambda_{dr} i_{qs} - \lambda_{qr} i_{ds}), \quad (4.10)$$

$$p\omega_m = \frac{1}{J} (T_e - T_m), \quad \omega_r = \frac{P}{2} \omega_m, \quad (4.11)$$

where the upper-case letter P denotes the number of poles, J is the moment of inertia, and T_e , T_m are the electromagnetic and mechanical torque of the machine, respectively. The implementation of the DCPVBR model of a Y-connected IM is demonstrated in Figure 4.2.

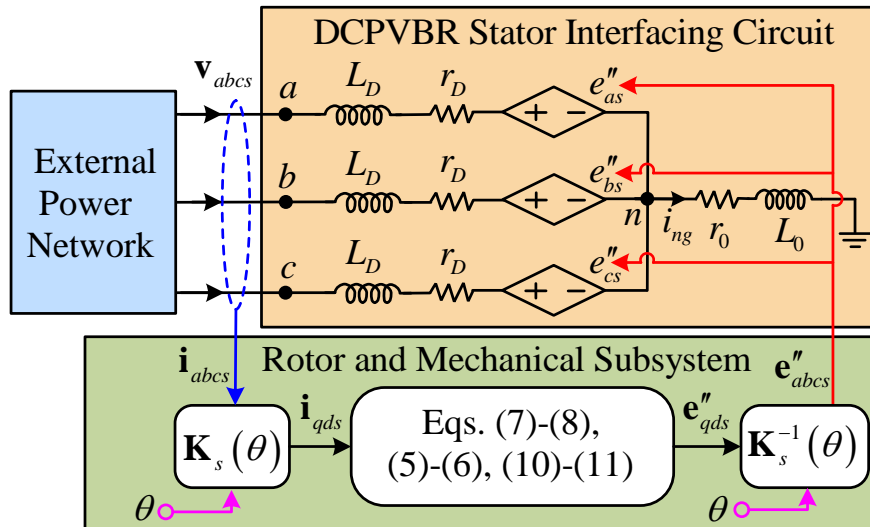


Figure 4.2 Implementation of the DCPVBR model of a three-phase Y-connected IM with decoupled and constant RL branches for stator interfacing circuit [18].

4.1.2 Universal High-Frequency Model [7]

The universal high-frequency model [7] was derived based on [34] using a single-section phase-belt winding equivalent circuit and is depicted in Figure 4.3 as a per-phase equivalent circuit.

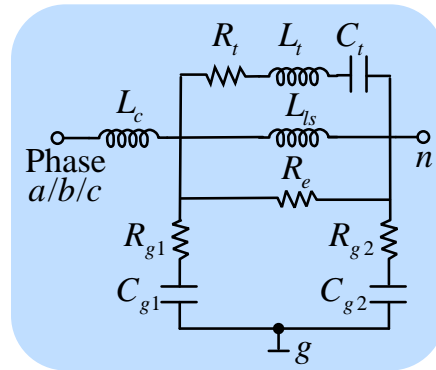


Figure 4.3 Per-phase equivalent circuit representations of the universal high-frequency induction machine model [7] for arbitrary stator windings connections.

As can be seen in Figure 4.3, it possesses a simple and unified structure for representing arbitrary stator winding configurations such as Y-, Δ -, series-, and parallel- for induction machines. Additionally, the associated parameters have physical definitions and importance [7], [34]. Specifically, C_{g1} and C_{g2} represent the phase-ground and neutral-ground equivalent stray capacitances, respectively; R_{g1} and R_{g2} represent the copper skin-effect and proximity-effect resistances; L_{ls} represents the stator leakage inductance; R_e accounts for power losses due to high-frequency eddy-currents; and the series branch elements R_t , L_t , and C_t capture the second resonance in the measured DM impedance as a result of the stator windings' inter-turn capacitive effects. Notably, at mid-high frequencies, the voltage distribution throughout different coils of the stator windings becomes non-uniform [51], which causes the entire surge to fall in the first few turns of the coils [21], [51]. In the universal model [7], the effects of the combined stator leakage

inductance of the first few turns and the internal feed conductors are incorporated using the inductance L_c , as shown in Fig. 4.3. This model also does not consider the phase-phase capacitive couplings, which sometimes can be neglected [27].

The universal high-frequency IM model has a straightforward parameterization procedure, details of which can be found in [7], although the parameters are influenced by different machine stator winding configurations [7]. Generally, the DM and CM impedances are considered to parametrize the high-frequency IM model and deemed effective in analyzing its behaviour in a wide frequency range. It was also noted that the DM impedance strongly influences the reflected overvoltage ringings [7], whereas bearing or shaft voltages/currents are strongly influenced by the CM impedance [21]. Therefore, accurately representing the DM and CM impedances is critical for predicting the high-frequency phenomena associated with the VFDs.

Typically, the DM and CM impedances are measured when the machine is disconnected from the ac supply and is at a standstill [7], [21], [28], [33], [34] because the rotor speed and stator currents have no significant impact on these measured impedances in the mid-to-high frequency range [7], [11], [21], [33], [34]. The DM impedance is obtained by shorting two phases of the stator windings and measuring the impedance between them and the third phase, as illustrated in Fig. 4.4(a). An impedance analyzer, frequency response analyzer, or network analyzer can be used for this purpose. The CM impedance is obtained by connecting all three phases of the stator windings together and measuring the impedance between them and the motor frame, as illustrated in Fig. 4.4(b). These measured DM and CM impedances depend on different machine stator winding configurations and machine geometry [7], [32], [34].

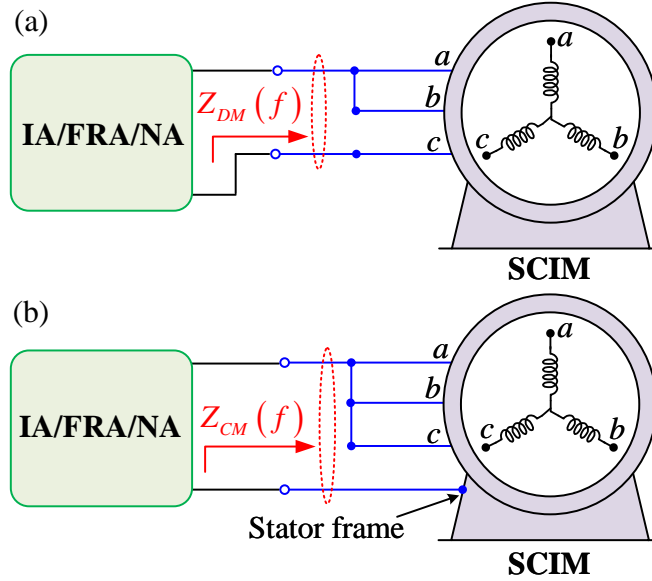


Figure 4.4 Setup arrangement for measuring the impedance characteristics of a three-phase squirrel-cage IM: (a) DM impedance (Z_{DM}) (b) CM impedance (Z_{CM}).

According to the arrangements in Figure 4.4, universal HF CM and DM equivalent circuits can be realized based on the per-phase equivalent circuit in Fig 4.3, as demonstrated in Figure 4.5. It is noted that this model can accurately depict the DM impedances in the mid-high frequency range (i.e. 50 kHz – 10 MHz) [7]. However, some discrepancies in the DM impedances at the low frequency were observed in this model. Moreover, the model [7] also does not predict the bearing voltages, ripples in currents, and torque waveforms due to the changes in motor slip and loading effects. At the same time, this type of phase belt-winding model configuration offers a good fit for fast motor phase voltage changes, and CM current calculation using this model is much closer to the measurements [32]. Because of these features, this universal high-frequency model may be integrated with the low-frequency full-order model.

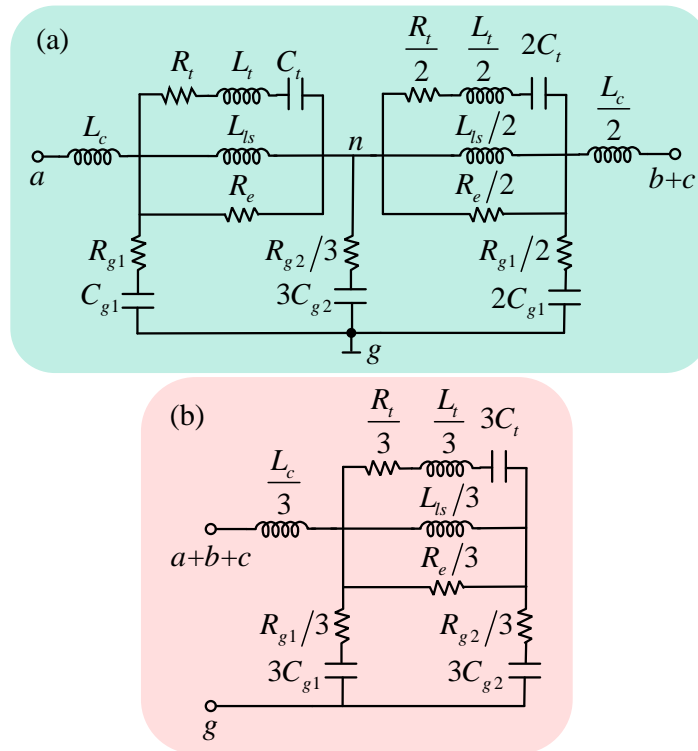


Figure 4.5 The differential and common mode universal high-frequency equivalent circuits of the induction machine (a) DM equivalent circuit (b) CM equivalent circuit.

4.1.3 High-Frequency Bearing Circuit Model [38], [39]

The cross-section of an electrical machine depicting the high-frequency inverter-induced bearing voltage and currents is shown in Figure 4.6(a).

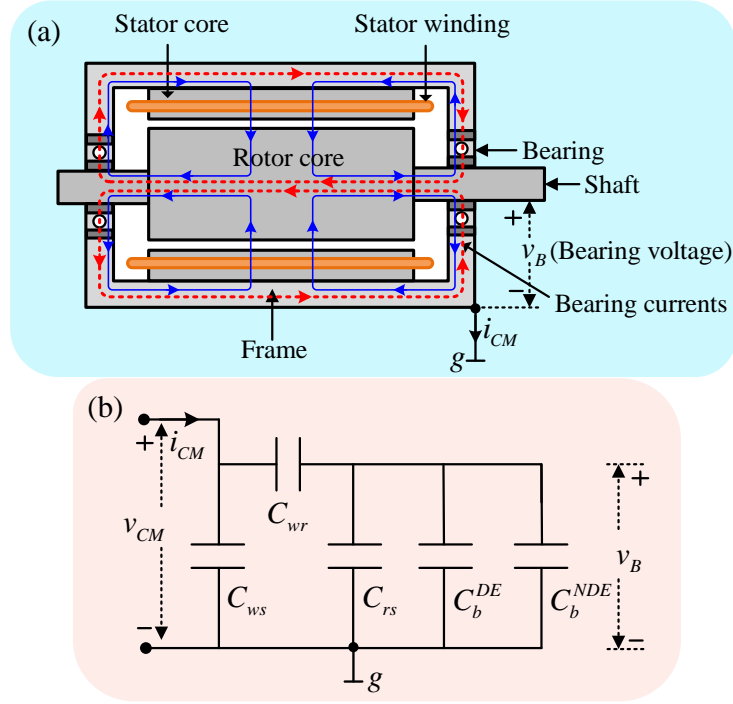


Figure 4.6 High-Frequency bearing phenomenon (a) cross-section of electrical machine depicting induced bearing voltage and currents (b) equivalent high-frequency bearing circuit model [38], [39]

Based on Figure 4.6, it is noted that the induced CM voltage strongly influences the bearing voltage/currents. As a result, a lumped-parameter equivalent bearing circuit model was proposed in [38], [39] in the form of a capacitive voltage divider circuit consisting of several HF stray capacitances, as illustrated in Figure 4.6(b). Specifically, the bearing voltage mirrors the CM voltage waveforms based on the adopted modulation schemes through the bearing voltage ratio (BVR) as

$$v_B = \underbrace{\left(\frac{C_{wr}}{C_{wr} + C_{rs} + C_b^{DE} + C_b^{NDE}} \right)}_{\text{BVR}} \times v_{CM}, \quad (4.12)$$

These stray capacitances in (4.12) and the bearing circuit model of Figure 4.6(b) and (4.12) have physical significance. Specifically, C_{ws} represents the winding-to-stator frame stray

capacitance, C_{wr} represents the winding-to-rotor stray capacitance, C_{rs} represents the rotor-to-stator frame stray capacitance, C_{bDE} and C_{bNDE} represent the bearing stray capacitances at the drive and non-drive ends [38], [39]. Various methods can be employed to extract these parameters, e.g., analytically based on design [39], experimentally [35], or through FEA methods [37], [38].

4.1.4 Proposed Wide-Band DCPVBR Model

To address the limitations of the prior/existing models of IMs, a wide-band constant-parameter voltage-behind reactance (WBCPVBR) is proposed, which integrates the advantageous properties of the low-frequency DCPVBR model [18], universal high-frequency model [7], as well as bearing circuit model [39]. The term “wide-band” refers to the capability of the model to represent the machine’s DM and CM behaviour over a wide range of frequencies (~dc to 10MHz). The equivalent circuit and implementation of the proposed WBDCPVBR model are shown in Figure 4.7.

As seen in Figure 4.7, the proposed WBDCPVBR model merges the stator interfacing circuits of the low-frequency DCPVBR model in Figure 4.2 and the universal high-frequency model in Figure 4.3. Specifically, most part of the high-frequency model is conveniently added on top of the low-frequency model, except that the stator winding leakage inductance L_{ls} of the high-frequency model is omitted because its effect is already taken into account in the interfacing inductance L_D of the low-frequency model. The rotor and mechanical subsystems are based on the DCPVBR model, which computes the sub-transient back-EMFs, based on (4.5)–(4.8), as inputs to the controlled voltage sources in the stator interfacing circuit. It is worth noting that, at the mid-high frequencies, the magnetic flux penetration into the rotor of the squirrel-cage IMs is minimal [21], [33], [34].

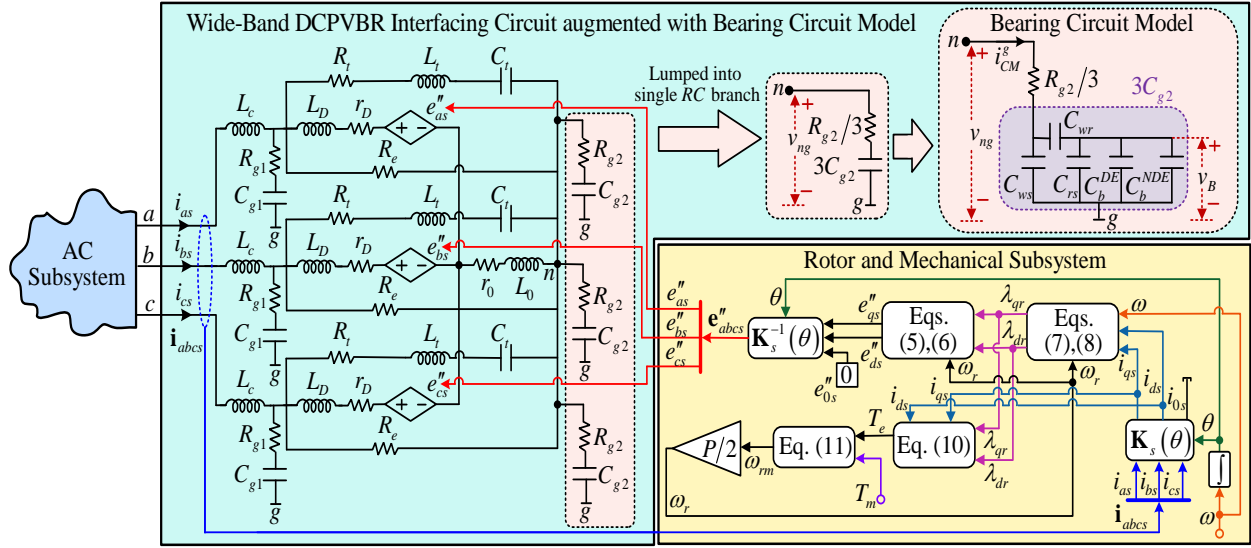


Figure 4.7 Implementation of the proposed WBDCPVBR model of induction machines augmented with bearing circuit model.

Therefore, the low-frequency parameters can be used for the rotor subsystem and remain unchanged in the mid-high frequency range [21], [33].

The proposed WBDCPVBR model also includes the lumped-parameter bearing equivalent circuit of Figure 4.6 to predict the effect of high frequency bearing voltage and CM currents phenomena induced through stray capacitances. This is done by representing the branch consisting of a parallel combination of the stator high-frequency R_{g2} and C_{g2} elements as the equivalent bearing circuit of Figure 4.6, shown in the red-highlighted boxes in Figure 4.7.

In agreement with the LF-DCPVBR and universal high-frequency models, the parameters associated with the proposed WBDCPVBR model possess the same physical significance, whose parametrization procedure is also very simple and straightforward. For example, the low-frequency parameters can be extracted based on the standard DC resistance, blocked rotor, and no-load tests on the induction machine [43], similar to [18]. Also, the high-frequency parameters can be

extracted from the corresponding measured DM and CM impedances of the induction machine, similar to the parametrization method for the universal high-frequency model [7]. Additionally, with the inclusion of the zero-sequence branch in the proposed WBDCPVBR model, the zero sequence currents will be zero for a balanced three-phase system and non-zero for an unbalanced system, which is consistent with its physical meaning and DCPVBR model structure.

Overall, the proposed WBDCPVBR model possesses a convenient structure and interfacing circuit using a constant parameter, decoupled RLC branches, and controlled voltage sources. When implemented in EMT simulation programs, these advantageous structural properties enable its efficient and direct interface with arbitrary external networks.

4.2 Model Validation

To verify the effectiveness of the proposed WBDCPVBR model, a VFD system shown in Figure 4.1 is considered, where a three-phase 4-pole, dual-voltage (230V/460V), nine-lead, 7.5hp squirrel cage IM (Model: Baldor EM3710T) is connected to an ABB drive (ACS150-03U-09A8-2) through using power cables.

The experimental laboratory setup is shown in Figure 4.8. Appendix C of this thesis summarizes the system data, including the low-, high-frequency, and bearing circuit parameters for the subject series-Y and parallel-Y IM stator winding configurations. For computer studies and comparisons with experimental measurements, the case-study system has also been implemented in MATLAB/Simulink using the proposed WBDCPVBR model for the IM and its conventional/existing counterpart models, i.e., low-frequency DCPVBR [18] and universal HF models [7].



Figure 4.8 Experimental laboratory setup of the VFD system: (1) ABB ACS150 drive with safety block, (2) power cable, (3) three-phase 7.5hp Baldor EM3710T IM with arbitrary stator windings connections and terminal voltages measurement setup, (4) bearing voltages measurement setup; (5) oscilloscope for displaying and recording output waveforms; (6) phase and CM currents measurement setup.

4.2.1 Experimental Verification of DM and CM Impedances

The DM and CM impedance response characteristics of the proposed WBDCPVBR model are verified here against the existing IM models and experimental measurements. It is considered that the rotor is at a standstill, and the stator terminals are disconnected from the three-phase AC power supply for impedance extraction.

Herein for reference purposes, the measured DM and CM impedances of the subject IM series-Y winding connection have been obtained from 100 Hz to 10 MHz using a network analyzer (VNA) according to Figure 4.4. The resulting DM and CM impedance response characteristics

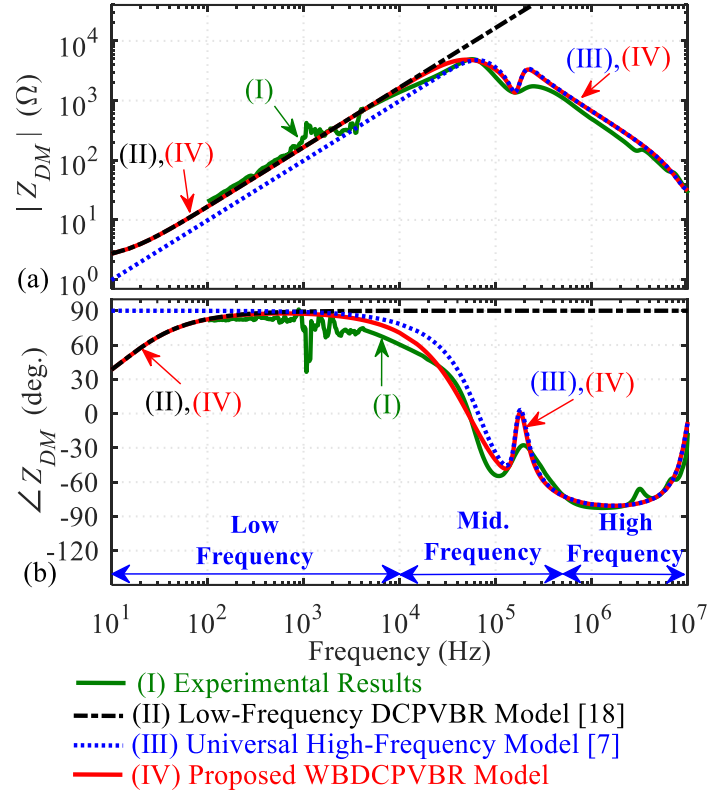


Figure 4.9 Superimposed measured and simulated DM impedance characteristics of the proposed WBDCPVBR model for series-Y winding connection: (a) DM Magnitude, and (b) DM Phase.

(i.e. magnitude and phase spectrums) are shown in Figures 4.9-4.10, respectively. In the same figure, the simulation results of the low-frequency DCPVBR, universal HF, and proposed WBDCPVBR IM models are superimposed with the experimental results. These impedance response characteristics are divided into three regions, namely low-frequency range (10 Hz-100 kHz), mid-frequency range (100 kHz-500 kHz), and high-frequency range (500 kHz-10 MHz).

As observed in Figure 4.9(a),(b), the DM impedance shows inductive behaviour in the low-mid frequency range (i.e. 10 Hz-50 kHz) with its corresponding phase starting from around 38° (for LF-DCPVBR and proposed WBDCPVBR models at 10 Hz) and 81° (for measurement results at 100 Hz). However, the DM impedance starts to demonstrate a capacitive behaviour in the high-

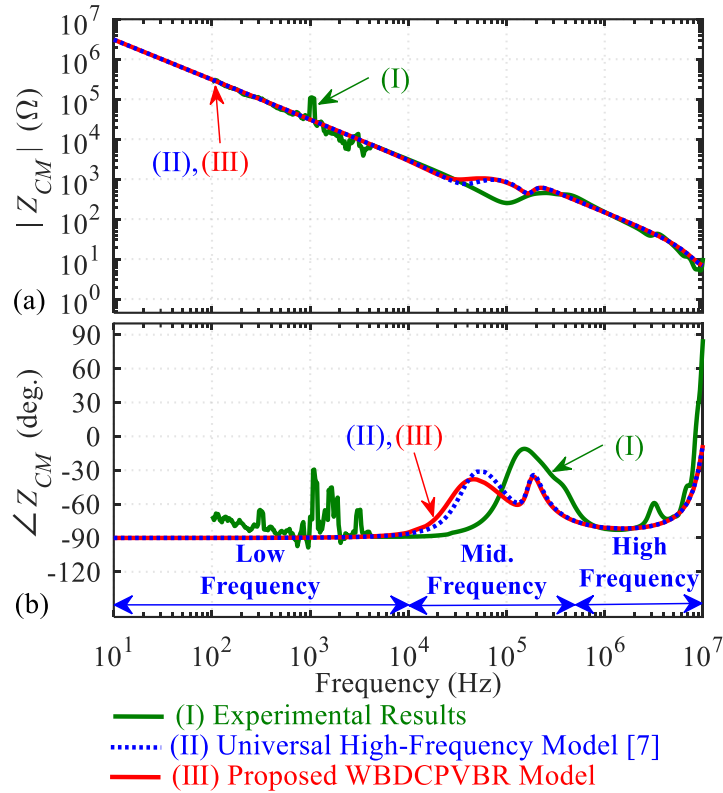


Figure 4.10 Superimposed measured and simulated CM impedance characteristics of the proposed WBDCPVBR model for series-Y winding connection: (a) CM Magnitude, and (b) CM Phase.

frequency range (i.e. 500 kHz-10 MHz) with its corresponding phase angle ending around -7.4° (for universal HF and proposed WBDCPVBR models at 10 MHz) and 18° (for measurement results at 10 MHz). Whereas in the mid-frequency range, DM impedances alternate between inductive and capacitive behaviour. While, as observed in Figure 4.10(a),(b), the CM impedances overall behave capacitively in major frequency regions with few exceptions at mid frequencies due to resonance phenomenon and as reflected by corresponding negative phase angles starting from around -90° (for universal HF and proposed WBDCPVBR models at 10 Hz) and -75° (for measurement results at 100 Hz).

It was also observed in Figures 4.9-4.10 that the LF-DCPVBR model accurately predicts the DM impedances only in the low-frequency range and does not predict DM impedance in the mid-high frequency range. In addition, the LF-DCPVBR model also does not predict the CM impedances in the entire spectrum due to the lack of stator frame connection point and open-circuit in the LF-DCPVBR model for extracting CM impedance using the setup in Figure 4.4(b). On the other hand, the universal high-frequency model predicts the CM impedances reasonably well in the wide frequency range. However, the universal HF model accurately captures the DM impedances only at mid-high frequencies and gives a noticeable error in the low-frequency range. Meanwhile, the proposed WBDCPVBR model offers higher accuracy than other models and can accurately capture the machine's measured DM and CM impedances across almost the entire frequency spectrum from ~dc to 10 MHz. Moreover, the proposed WBDCPVBR model exhibits consistent behaviour and accurately matches the experimental impedance measurements while having an excellent agreement between the LF-DCPVBR model results (i.e. in the low-frequency range) and universal high-frequency model results (i.e. in the mid-high frequency range).

However, there is a slight difference in the DM and CM impedances between the experimental and simulated results at some frequencies in the mid-frequency range, but its accuracy can be further improved by utilizing advanced parameter optimization methods to estimate model parameters with higher accuracy.

Therefore, it is concluded that frequency domain impedance analysis results verify the effectiveness of the proposed WBDCPVBR model in accurately predicting the wide-band impedance characteristics from ~dc to 10 MHz, consistent with the experimental measurements and showing improvements over conventional/existing models.

4.2.2 High-Frequency DM and CM Analysis in VFD System

Here, a test case study has been carried out on a short cable-fed induction machine drive system to validate high-frequency DM and CM response in the time domain. It is assumed that the machine operates under the steady state and no-load condition (approximately corresponding to 40Hz stator input frequency). The measurements are taken from the experimental setup in Figure 4.8 when the IM is configured in parallel-Y stator windings and is driven by the ABB VFD through a short cable of 1m length. The VFD has a two-level inverter topology, and its switching frequency is 4kHz. The CM ground current is measured with a current probe as the current flows out of the motor frame to the floating ground point of the VFD. The bearing voltage is measured with carbon brushes through the AEGIS's bearing voltage measurements test setup mounted on the machine shaft as the potential difference between the shaft at the drive-end and machine stator frame, as shown in Figure 4.8.

For adequate comparison, the phase-to-ground voltages v_{abcg} of the three-phase VFD output are measured from experiments and then fed into the MATLAB/Simulink simulation using the controlled voltage sources for the proposed model verification. The waveforms comparison of the system variables, i.e. phase a current, neutral-ground voltage, bearing voltage, CM and DM currents as obtained from experimental measurements and proposed WBDCPVBR model simulated with a $0.1\mu\text{s}$ time-step using *ode4* solver are presented in Figures 4.11-4.13, respectively.

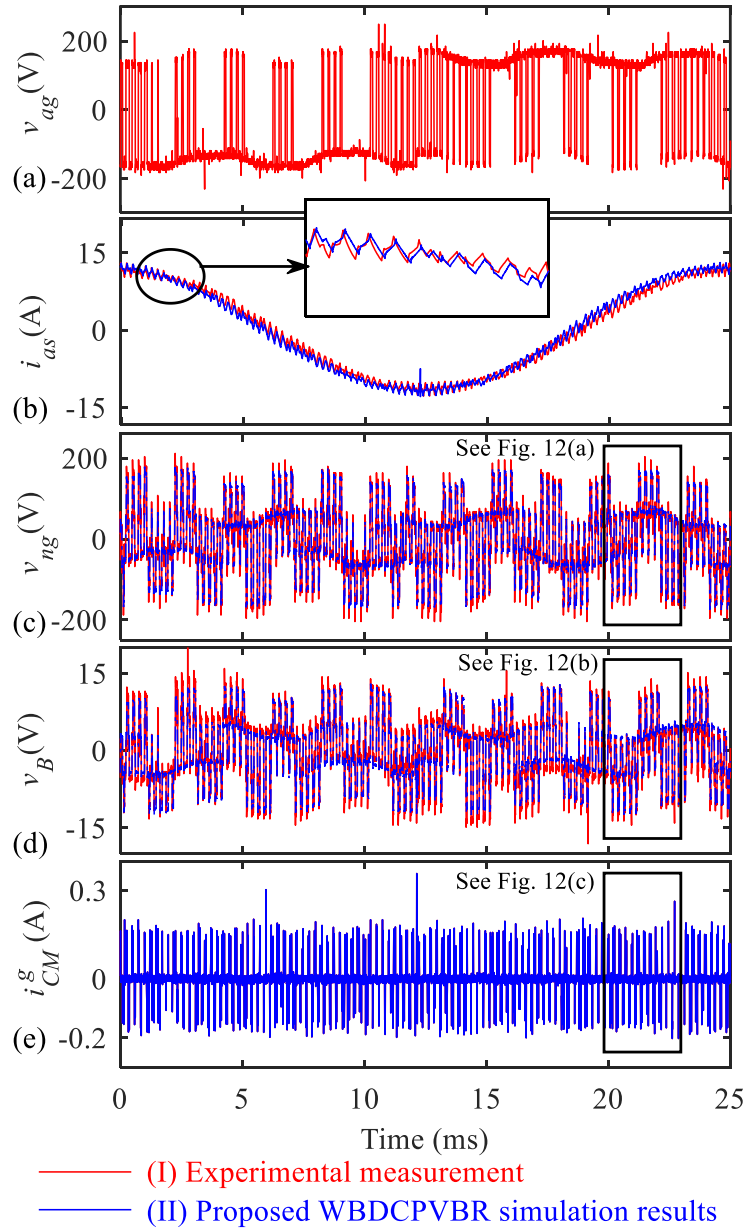


Figure 4.11 Response of several system variables as obtained by the experimental measurements and proposed model under no-load condition for 1m power cable: (a) v_{ag} , (b) v_{ab} , (c) i_{as} , (d) v_{ng} , (e) v_B , and (f) i_{CM} .

As observed in Figures 4.11-4.13, the proposed WBDCPVBR model yields a reasonably accurate prediction of corresponding system variables, and simulation results are in good agreement with the experimental measurements. Since the short cables are used (and the

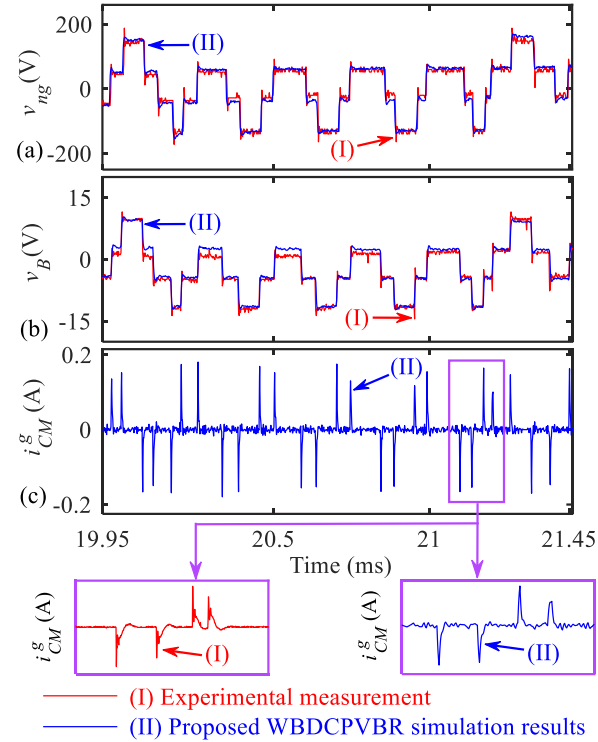


Figure 4.12 Magnified view of the corresponding variables from Figure 4.11 as obtained by the experimental measurements and proposed model under no-load condition for 1m power cable: (a) v_{ng} , (b) v_B , and (c) i_{CM} .

ABB VFD does not have WBG semiconductor devices), and over-voltage reflections are not pronounced in the results in Figures 4.11-4.13. Moreover, it is also seen that measured phase-ground voltages are asymmetrical, i.e. slightly changing, which is due to floating ground point (i.e. middle point between DC link capacitors C_1 and C_2) and varying DC link capacitor voltage between $\pm 177V$ in the ABB VFD system.

The observed CM current in Figures 4.11(e) and 4.12(c) have spikes and are capacitive in nature, which is typically due to switching and capacitive coupling among the phases and ground terminals in the IM. Also, the observed ripples in the phase current waveform achieved by the proposed model are reasonably close to the experimental measurements, as shown in Figure 4.11(b).

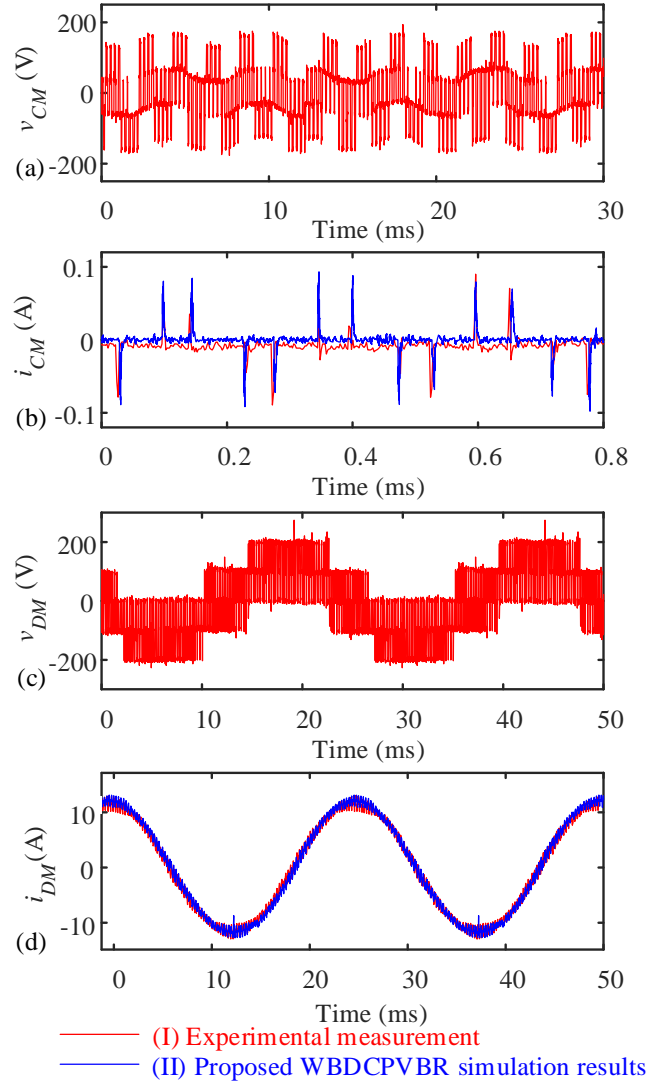


Figure 4.13 CM and DM response of parallel-Y IM configuration as obtained by the experimental measurements and proposed WBDCPVBR model under no-load condition for 1m power cable: (a) v_{CM} , (b) i_{CM} , (c) v_{DM} , and (d) i_{DM} .

It is also observed from Figures 4.11-4.13 that bearing voltage mirrors the CM voltage v_{CM} and neutral-to-ground voltage v_{ng} through an appropriate bearing-voltage-ratio (BVR) such that $v_B = \text{BVR} \times v_{CM}$, and it can be readily predicted by the proposed WBDCPVBR model augmented with capacitive voltage divider bearing circuit. The BVR of the subject 7.5hp IM was calculated

to be approximately equal to 13-14%. It is noted that CM and neutral-to-ground voltages are equal in a balanced three-phase system and slightly different in an unbalanced system.

The accuracy of the proposed model can be further confirmed from the magnified plot comparisons of selected variables, i.e. neutral-to-ground voltage, bearing voltage, and CM ground current, as depicted in Figure 4.12. Therein, it is observed that the proposed model results closely match the experimental measurements despite a small error, mainly introduced due to high-frequency DM and CM impedances fitting.

Furthermore, Figure 4.13(a)-(d) demonstrates the agreement between measured and simulated waveforms of the CM and DM currents components of the IM-drive system, which are calculated from the typical DM and CM formulas as listed in Appendix C of this thesis. It is also worth noting that the fundamental component at 40 Hz of the DM voltage waveform, as shown in Figure 4.13(c) for parallel-Y IM winding connection, is calculated to be 72.9 V_{rms}. The fundamental component of DM current, as shown in Figure 4.13(d), obtained by the proposed model was calculated to be 7.4 A_{rms}, which results in a DM impedance of 9.8 Ω at 40 Hz frequency. However, considering the motor standstill condition, the fundamental component of the proposed model simulated DM current becomes 42.8 A_{rms}, thus resulting in a DM impedance of 1.7 Ω at 40 Hz, which is consistent with the DM impedance response characteristics of the proposed WBDCPVBR and LFBVBR model at 40 Hz as shown in Figure 4.9(a) e.g. $Z_{DM}^{series-Y} = 4 \times Z_{DM}^{parallel-Y}$ (in low-frequency range). This case study verifies the accuracy of the proposed WBDCPVBR model in time-domain simulation of the short-cable fed IM drive system against the experimental results.

4.2.3 Reflected Over-Voltage Analysis in Long-Cable Fed IM Drive System

Next, to demonstrate the reflected transient overvoltage phenomenon caused due to wave propagation effects in the long cable-fed IM drive system, a parallel-Y configuration of a 7.5hp Baldor motor is considered in this case study. The measured waveforms of the phase-to-ground voltages and bearing voltage for a cable of 50m used in this long-cable-fed IM-drive study are presented in Figure 4.14. As seen in Figure 4.14, the over-voltage ringing waveforms with peaks roughly equal to 1.79 times the reference DC link voltage are observed, which is due to high-frequency oscillations between the motor and power cables.

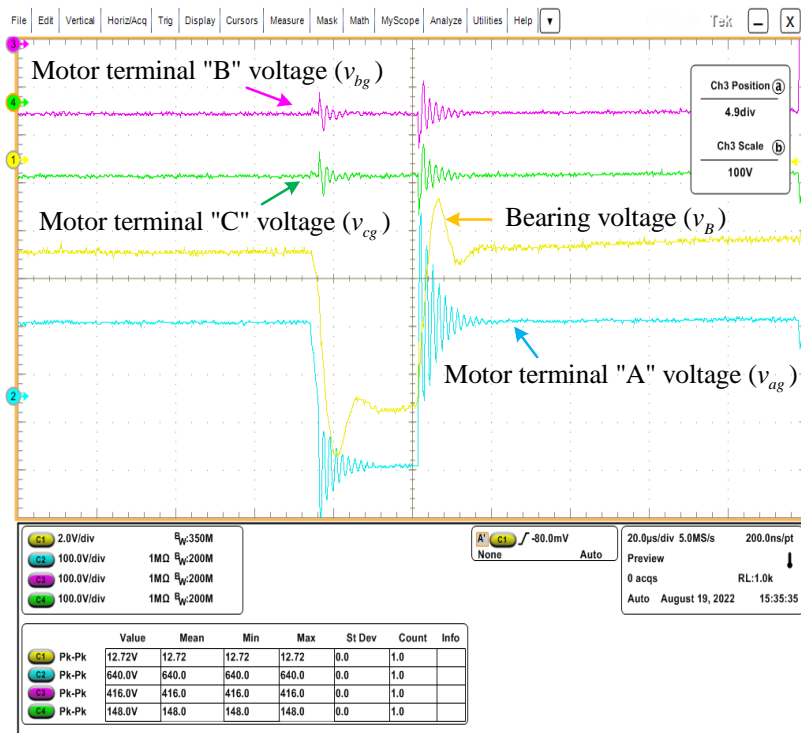


Figure 4.14 Measured reflected over-voltage waveforms at the motor terminals and bearing/shaft when using 50m power cable.

A decoupled single-line high-frequency behavioural circuit model of the cable has been previously proposed in the literature [34]. A three-phase behavioural circuit high-frequency model of three-phase power cables requires a separate dedicated publication, which is out of scope for this thesis. Therefore, a three-phase distributed parameter line model component of length 50 m in the Simscape Electrical toolbox is inserted in between the recorded three-phase ABB motor drive's voltages sources and the proposed three-phase WBDCPVBR model to emulate the response of long-cable-fed IM drive system. The resulting simulated response of phase-ground voltages, neutral-ground voltage, and bearing voltage as obtained by the proposed model simulated with $0.1\mu\text{s}$ time-step using *ode4* solver are depicted in Figure 4.15, wherein over-voltage reflections across machine terminals' voltage waveforms are clearly visible. However, the overvoltage ringing phenomenon can become more pronounced when the three-phase cable model is more accurate and parametrized properly for fair and accurate comparisons.

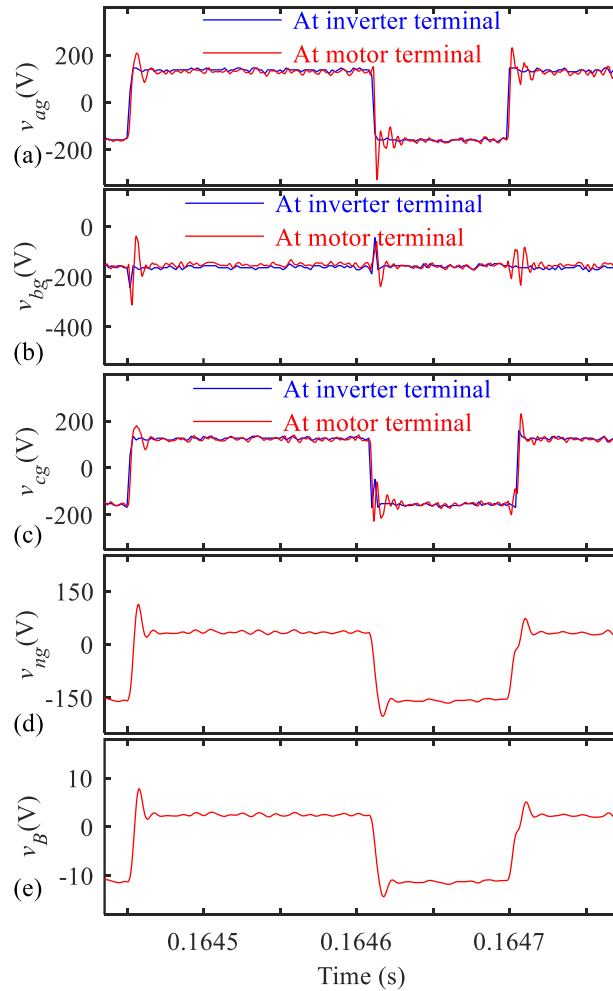


Figure 4.15 Reflected over-voltage waveforms at the motor terminals and bearing/shaft for 50m power cable as obtained by the proposed model: (a) v_{ag} , (b) v_{bg} , (c) v_{cg} , (d) v_{ng} , and (e) v_B .

It is predicted that the proposed WBDCPVBR model can yield more accurate simulation results when an accurate high-frequency three-phase high-frequency cable model is used instead of frequency independent three-phase distributed parameter line model available in the Simscape Electrical toolbox.

Finally, it is deduced that the proposed WBDCPVBR model offers significant advantages over these existing models in terms of its versatile features such as direct and efficient machine

network interface, simple structure and straightforward parameterization procedure, appreciable improvement in predicting several transient and steady-state responses of system variables from ~dc to 10 MHz as well as under different loading conditions. Due to these versatile advantageous features, it is envisioned that the proposed WBDCPVBR model can be a very useful asset for induction machine drive studies in many offline and/or real-time state-variable-based EMT simulation programs.

Chapter 5: Conclusion

The presented research work in this thesis concentrated on advancing the state-of-the-art modelling of IM-converter systems for their accurate and efficient simulations in EMT programs. The VFDs of different low- and high-power levels are widely utilized in many commercial, industrial, vehicular, and propulsion applications, wherein typically, a squirrel-cage IM is fed from an inverter through a cable. Modelling and simulating such motor-drive systems is essential for designing and operating all such applications and products. This thesis makes several contributions to this research domain while achieving its original objectives.

5.1 Contributions

Objective I of this thesis is accomplished in Chapter 2, where the numerical performance of several combinations of machine-converter models was investigated for offline and real-time simulation of VFD systems in SVB EMT simulators. Conventional simulations of VFD systems are carried out using detailed switching models of VSIs combined with classical $qd0$ IM models. Such detailed VSI models connected with $qd0$ IM models require interfacing snubbers and small time steps, thus making them computationally expensive. At the same time, for many system-level studies that are focused only on low-frequency electromechanical interactions, the average-value models of the VSIs may be used more effectively. Also, the VBR machine models may offer some advantages in terms of interfacing with converter circuits. Chapter 2 presents simulation studies utilizing several combinations of machine-converter models conducted in MATLAB-Simulink and real-time OPALRT5700 simulator. It has been verified that the AVM VSI–built-in $qd0$ IM model loses its accuracy at around a time-step size of 100 μ s. In contrast, the new AVM VSI–DCPVBR IM model yields stable and accurate solution results even with a large time-step size of

300 μs . Meanwhile, the DI-AVM VSI–custom-built- $qd0$ IM model delivers the best and most accurate results with a large time-step size of 350 μs . However, this model is less practical in EMT packages as it requires building a custom $qd0$ IM model to include network impedance in its stator branches. Additionally, it has been validated that both the DI-AVM VSI–custom-built- $qd0$ IM and new AVM VSI–DCPVBR IM models give significant computational advantages by enabling real-time and offline simulations with time-step up to $\sim 300\text{-}350$ μs (an improvement by a factor of 3 to 3.5) while maintaining acceptable accuracy. This results in a very low CPU usage of 0.4% and 0.56% on the OP5700 real-time simulator by these two models, making them most suited for system-level electromechanical and control-type studies.

Objective II is achieved in Chapter 3 by presenting a reconfigurable star-delta CPVBR model for a three-phase squirrel-cage induction machine. This was done by employing the advantageous properties of the CPVBR models to switch between the star and delta stator winding configurations under different operating conditions. The low-frequency deep-rotor-bar phenomenon has been considered by utilizing linear approximation for a speed-dependent rotor resistance which offers enhanced accuracy in predicting motor starting transients. The improved star-delta CPVBR model is validated through computer studies against the $qd0$ model in MATLAB/Simulink, and is shown to offer superior simulation performance in terms of reduced CPU time (3.4 s vs 264.2 s), fewer steps (13,177 versus 3,122,687) and larger average time-step size (258 μs vs 84.6 μs) using *ode45* variable time-step solver. It is also demonstrated that the proposed star-delta CPVBR model results in a more accurate prediction of star-delta switching transitions and steady-state operation (compared to the conventional $qd0$ that must use artificial snubbers). It is envisioned that the presented reconfigurable star-delta CPVBR model can be

utilized in EMT simulators to study star-delta starting transients in industrial factories, mining sites, and marine power systems with large induction motors.

Objective III is addressed in Chapter 4 of the thesis by developing a wideband, decoupled constant-parameter VBR model for representing a three-phase squirrel-cage induction machine model that is valid from \sim dc to 10 MHz. This has been achieved by incorporating the low-frequency DCPVBR, the universal high-frequency, and the bearing circuit models into the three-phase equivalent circuit of the proposed model. The proposed model is validated using computer simulations and experimental results obtained from a typical 7.5 hp induction motor connected to a drive system through a cable. It is demonstrated that the proposed model can predict various phenomena associated with VFD systems, such as DM and CM impedances, reflected wave transient over-voltages, and bearing/shaft voltages and currents. Additionally, the proposed WBDCPVBR model offers significant advantages over these existing models in terms of its features, such as direct machine-network interface, simple structure, straightforward parameterization procedure, and accuracy in a wide range of frequencies \sim dc to 10 MHz. To provide the reader with a comprehensive overview, Table 5.1 summarizes the salient features of the proposed IM model with respect to the existing state-of-the-art models explained in Chapter 1, Section 1.2. This table now includes an additional column (on the right side) that lists the properties of the proposed model, which presents the most complete combination of the desired features. Due to these features, it is envisioned that the proposed model will become a valuable asset for studying VFD systems and machine-converter interactions in marine power systems, mining and oil drilling sites.

Table 5.1 Summary of features of the proposed induction machine model with respect to the existing state-of-the-art models

Models	PD [15], [16]	<i>qd0</i> [17]	VBR [18]	[12], [25]–[28]	[20]	[7]	[21]	Proposed WBDCPVBR Model	
Structure	complex	simple	simple	complex	complex	simple	complex	simple	
Interfacing circuit	variable & direct	constant & indirect	constant & direct	constant & direct	constant & indirect	constant & direct	constant & direct	constant & direct	
Parameterization method	easy	easy	easy	complicated	complicated	easy	complicated	easy	
Valid frequency range (Hz)	~DC-5k	~DC-5k	~DC-5k	~5k~10M	~1k~50k	50k-10M	10-10M	~DC-10M	
Low-frequency behaviour	Transient	Yes	Yes	Yes	No	Yes	No	Yes	
	Steady-state	Yes	Yes	Yes	No	Yes	No	Yes	
	Motor slip variation	Yes	Yes	Yes	No	Yes	No	Yes	
High-frequency behaviour	Transient	No	No	No	Yes	Yes	Yes	Yes	
	Steady-state	No	No	No	Yes	Yes	Yes	Yes	
	DM impedance	low-freq. range	low-freq. range	low-freq. range	mid-high freq. range	–	mid-high freq. range	low-high freq. range	low-high freq. range
	CM impedance	No	No	No	Yes	–	Yes	Yes	Yes
	CM current	No	No	No	–	–	No	No	Yes
	Reflected over-voltages	No	No	No	Yes	–	Yes	Yes	Yes
	Bearing voltages	No	No	No	No	No	No	Yes	Yes

5.2 Anticipated Impact

The efficient modelling approach presented in **Chapter 2** holds significant potential in advancing system-level studies of marine power and propulsion systems involving many motors, converters, and electromechanical components. The reconfigurable star-delta CPVBR model, as presented in **Chapter 3**, is highly desirable for analyzing and optimizing the IM's starting and operational performance during motor starting, star-delta switching transients, and regular operation. Therefore, this model is projected to be utilized in the EMT simulators for conducting such studies. The WBDCPVBR model, as presented in **Chapter 4**, offers significant advantages over the existing IM models in terms of its several features, as outlined in Table 5.1. A model with such capabilities will be particularly useful for studying the machine-converter interactions and induced bearing voltage phenomenon in marine propulsion applications, where it is critical to design controllers and implement mitigating measures to reduce all parasitic currents through the metal frames of motors that contribute to corrosion and equipment lifespan reduction.

It is also envisioned that all models presented in Chapters 2–5 will offer substantial benefits to researchers, engineers, and power system consulting firms who are using EMT simulators. Utilizing proposed state-of-the-art models, engineers can perform system-level EMT studies (i.e. including offline and real-time simulations) more efficiently, with higher accuracy, using less computational resources and time.

5.3 Future Work

The research work presented in this thesis offers opportunities for further exploration in several directions. Due to space limitations, four potential research directions that may be soon pursued by fellow students within our group are explained as follows:

Firstly, the WBDCPVBR model presented in this thesis assumes a Y-connected stator winding configuration of squirrel-cage IMs due to the decoupled stator branch interfacing circuit of the DCPVBR formulation. However, the stator winding can be reconfigured based on different requirements and applications. For this purpose, it is desirable to develop a model that will be suitable for arbitrary stator windings configurations, such as Y-, Δ -, series-, and parallel- windings connections. To the authors' knowledge, a generalized wideband CPVBR induction machine model for arbitrary stator winding configurations has not been proposed in the literature. Therefore, the research approach laid out in Chapter 4 can be extended to propose a generalized wideband CPVBR model capable of representing arbitrary stator winding connections.

Secondly, the WBDCPVBR model has been developed in SVB EMT simulation programs, specifically for single-rate simulations. It should be noted that the rotor and mechanical subsystem of the IM model have relatively slow dynamics, while the stator interfacing circuit of the WBDCPVBR model is subjected to very fast electromagnetic transients. Therefore, the rotor subsystem can be simulated with larger time steps while maintaining reasonable accuracy. Consequently, future research would be to develop a multi-rate simulation approach of the WBDCPVBR IM model in EMTP for its efficient implementation in both PSCAD and RSCAD tools.

Thirdly, the induction machine models introduced in this thesis did not consider magnetic saturation as the VFD may generally prevent over-saturation and operate in a constant flux region.

However, additional modelling details such as main flux saturation, leakage flux saturation, and air gap flux harmonics may be considered in the proposed WBDCPVBR model, which will enhance the fidelity and accuracy of the wideband IM models.

Finally, the high-frequency modelling approach of Chapter 4 can be readily applied to permanent-magnet synchronous motors (PMSMs) that are now becoming widely considered in vehicular and renewable energy applications, where such motors are controlled by inverters switching at 10th of kHz using new semiconductor devices. As an extension of this research, wideband synchronous machine models will be crucial for studying the synchronous machine-converter interactions, which will be a future research topic.

Bibliography

- [1] P. S. Kundur, *Power system stability and control*. McGraw-Hill, 1994.
- [2] A. T. de Almeida, F. J. T. E. Ferreira, and G. Baoming, “Beyond induction motors—technology trends to move up efficiency,” *IEEE Trans. Indus. Applications*, vol. 50, no. 3, pp. 2103–2114, Jun. 2014.
- [3] G. Tanuku and P. Pillay, “Emulation of an induction machine for unbalanced grid faults,” *IEEE Trans. Indus. Applications*, vol. 57, no. 5, pp. 4625–4635, Oct. 2021.
- [4] Z. Yin, Q. Hou, Y. Zhang, and Y. Zhang, “A sensorless predictive torque control for induction motor using ultra-local model,” in *Proc. 24th Int. Conf. on Electrical Machines and Systems (ICEMS)*, 2021, pp. 136–140.
- [5] K. Kumar, M. Marchesoni, Z. Maule, M. Passalacqua, F. Soso, and L. Vaccaro, “Currents and torque oscillations mitigation in high power induction motor drives,” in *Proc. IEEE 15th Int. Conf. Compatibility, Power Electronics and Power Engineering (CPE-POWERENG)*, 2021, pp. 1–5.
- [6] A. M. El-Refaie, “Motors/generators for traction/propulsion applications: A review”, *IEEE Trans. Veh. Technol.*, vol. 8, no. 1, pp. 90-99, Mar. 2013.
- [7] M. S. Toulabi, L. Wang, L. Bieber, S. Filizadeh, and J. Jatskevich, “A universal high-frequency induction machine model and characterization method for arbitrary stator winding connections,” *IEEE Trans. Energy Convers.*, vol. 34, no. 3, pp. 1164–1177, Sep. 2019.
- [8] S. Decker, C. Rollbühler, M. Brodatzki, F. Rehm, A. Liske, and M. Hiller, “Comparison of losses in small star- and delta-connected permanent magnet synchronous machines,” in

- Proc. 23rd European Conf. Power Electron. and Applications (EPE'21 ECCE Europe)*, 2021, pp.1–10.
- [9] J. Larabee, B. Pellegrino, and B. Flick, “Induction motor starting methods and issues,” in *Proc. Conference Papers Industry Applications Society 52nd Annual Petroleum and Chemical Industry Conference*, 2005, pp. 217–222.
- [10] G. Zigirkas and J. Kalomiros, “An embedded fuzzy controller for the soft-starting of low-voltage induction motors,” in *2015 IEEE 8th International Conference on Intelligent Data Acquisition and Advanced Computing Systems: Technology and Applications (IDAACS)*, 2015, pp. 22–27.
- [11] P. Xie, G. Vakil, and C. Gerada, “Electric drive systems with long feeder cables,” *IET Electr. Power Appl.*, vol. 14, no. 1, pp. 16–30, Jan. 2020.
- [12] J. Sun and L. Xing, “Parameterization of three-phase electric machine models for EMI simulation”, *IEEE Trans. Power Electron.*, vol. 29, no. 1, pp. 36–41, Jan. 2014.
- [13] C. Purcarea, P. Mutschler, O. Magdun, A. Rocks, and A. Binder, “Time domain simulation models for inverter-cable-motor system in electrical drives,” in *Proc. 13th Eur. Conf. Power Electron. Appl.*, pp. 1–10, 2009.
- [14] B. Narayanasamy, A. S. Sathyanarayanan, F. Luo, and C. Chen, “Reflected wave phenomenon in SiC motor drives: Consequences boundaries and mitigation,” *IEEE Trans. Power Electron.*, vol. 35, no. 10, pp. 10629–10642, Oct. 2020.
- [15] H. C. Stanley, “An analysis of the induction machine,” *Trans. Amer. Inst. Elect. Eng.*, vol. 57, no. 12, pp. 751–755, Dec. 1938.
- [16] J. R. Martí and T. O. Myers, “Phase-domain induction motor model for power system simulators,” in *Proc. IEEE Commun. Power Comput. Conf.*, vol. 2, pp. 276–282, May 1995.

- [17] P. C. Krause, O. Wasynczuk, S. D. Sudhoff, and S. Pekarek, *Analysis of electric machinery and drive systems*, 3rd Edition, IEEE Press, Piscataway, NJ, 2013.
- [18] L. Wang, J. Jatskevich, and S. D. Pekarek, “Modeling of induction machines using a voltage-behind-reactance formulation,” *IEEE Trans. Energy Convers.*, vol. 23, no. 2, pp. 382–392, Jun. 2008.
- [19] L. Wang et al., “Methods of interfacing rotating machine models in transient simulation programs,” *IEEE Trans. Power Del.*, vol. 25, no. 2, pp. 891–903, Apr. 2010.
- [20] S. D. Sudhoff, D. C. Aliprantis, B. T. Kuhn, and P. L. Chapman, “An induction machine model for predicting inverter-machine interaction,” *IEEE Trans. Energy Convers.*, vol. 17, no. 2, pp. 203–210, Jun. 2002.
- [21] B. Mirafzal, G. L. Skibinski, R. M. Tallam, D. W. Schlegel, and R. A. Lukaszewski, “Universal induction motor model with low-to-high frequency-response characteristics,” *IEEE Trans. Ind. Appl.*, vol. 43, no. 5, pp. 1233–1246, Sep./Oct. 2007.
- [22] T. Plazenet, T. Boileau, C. Caironi, and B. Nahid-Mobarakeh, “A comprehensive study on shaft voltages and bearing currents in rotating machines,” *IEEE Trans. Ind. Appl.*, vol. 54, no. 4, pp. 3749–3759, Jul./Aug. 2018.
- [23] F. A. Kharanaq, A. Emadi, and B. Bilgin, “Modeling of conducted emissions for EMI analysis of power converters: State-of-the-art review,” *IEEE Access*, vol. 8, pp. 189313–189325, 2020.
- [24] A. Moreira, T. Lipo, G. Venkataramanan, and S. Bernet, “High frequency modeling for cable and induction motor overvoltage studies in long cable drives”, in *Proc. IEEE Ind. Appl. Conf. 36th IAS Annu. Meeting*, vol. 3, pp. 1787–1794, 2001.

- [25] I. Stevanovic, B. Wunsch, and S. Skibin, "Behavioral high-frequency modeling of electrical motors," in *Proc. Appl. Power Electron. Expo. Conf.*, pp. 2547–2550, Mar. 2013.
- [26] E. Zhong and T. A. Lipo, "Improvements in EMC performance of inverter-fed motor drives," *IEEE Trans. Ind. Appl.*, vol. 31, no. 6, pp. 1247–1256, Nov. 1995.
- [27] G. Grandi, D. Casadei, and U. Reggiani, "Analysis of common- and differential-mode HF current components in PWM inverter-fed ac motors," in *Proc. IEEE Power Electron. Spec. Conf.*, pp. 1146–1151, 1998.
- [28] S.-P. Weber, E. Hoene, S. Guttowski, W. John, and H. Reichl, "Modeling induction machines for EMC-analysis," in *Proc. IEEE 35th Annu. Power Electron. Spec. Conf.*, vol. 1, pp. 94–98, 2004.
- [29] G. Grandi, D. Casadei, and A. Massarini, "High frequency lumped-parameter model for AC motor windings", in *Proc. Eur. Power Electron. Appl. Conf.*, vol. 2, pp. 578–583, 1997.
- [30] A. Boglietti and E. Carpaneto, "Induction motor high frequency model", in *Proc. IEEE Ind. Appl. Conf. 34th IAS Annu. Meeting*, vol. 3, pp. 1551–1558, 1999.
- [31] M. Schinkel, S. Weber, S. Guttowski, W. John, and H. Reichl, "Efficient HF modeling and model parameterization of induction machines for time and frequency domain simulations", in *Proc. 21st Annu. IEEE Appl. Power Electron. Expo. (APEC) Conf.*, pp. 1181–1186, Mar. 2006.
- [32] O. Magdun and A. Binder, "High-frequency induction machine modeling for common mode current and bearing voltage calculation," *IEEE Trans. Ind. Appl.*, vol. 50, no. 3, pp. 1780–1790, May/Jun. 2014.

- [33] B. Mirafzal, G. L. Skibinski, and R. M. Tallam, "Determination of parameters in the universal induction motor model," *IEEE Trans. Ind. Appl.*, vol. 45, no. 1, pp. 142–151, Jan./Feb. 2009.
- [34] L. Wang, C. Ngai-Man Ho, F. Canales, and J. Jatskevich, "High-frequency modeling of the long-cable-fed induction motor drive system using TLM approach for predicting overvoltage transients", *IEEE Trans. Power Electron.*, vol. 25, no. 10, pp. 2653–2664, Oct. 2010.
- [35] D. Busse, J. Erdman, R. J. Kerkman, D. Schlegel, and G. Skibinski, "Bearing currents and their relationship to PWM drives," *IEEE Trans. Power Electron.*, vol. 12, no. 2, pp. 243–252, Mar. 1997.
- [36] M. Asefi and J. Nazarzadeh, "Survey on high-frequency models of PWM electric drives for shaft voltage and bearing current analysis," *IET Elect. Syst. Transp.*, vol. 7, no. 3, pp. 179–189, 2017.
- [37] P. Han *et al.*, "On the modeling of bearing voltage and current in PWM converter-fed electric machines using electromagnetic finite element analysis," in *Proc. 2021 IEEE Energy Convers. Cong. Expo. (ECCE)*, pp. 4606–4610, 2021.
- [38] P. Han, G. Heins, D. Patterson, M. Thiele, and D. M. Ionel, "Modeling of bearing voltage in electric machines based on electromagnetic FEA and measured bearing capacitance", *IEEE Trans. Indus. Appl.*, vol. 57, no. 5, pp. 4765–4775, Jun. 2021.
- [39] A. Muetze and A. Binder, "Calculation of motor capacitances for prediction of the voltage across the bearings in machines of inverter-based drive systems," *IEEE Trans. Ind. Appl.*, vol. 43, no. 3, pp. 665–672, May/Jun. 2007.

- [40] J. M. Erdman, R. J. Kerkman, D. W. Schlegel, and G. L. Skibinski, "Effect of PWM inverters on AC motor bearing currents and shaft voltages," *IEEE Trans. Ind. Appl.*, vol. 32, no. 2, pp. 250–259, Mar./Apr. 1996.
- [41] S. Quabeck, V. Grau, and R. W. De Doncker, "Modeling and mitigation of bearing currents in electrical traction drives," in *Proc. IEEE 23rd Int. Elect. Mach. Syst. Conf.*, pp. 1101–1106, 2020.
- [42] L. Ran, S. Gokani, J. Clare, K. J. Bradley, and C. Christopoulos, "Conducted electromagnetic emissions in induction motor drive systems part I. Time domain analysis and identification of dominant modes," *IEEE Trans. Power Electron.*, vol. 13, no. 4, pp. 757–767, Jul. 1998.
- [43] IEEE, 112-2017, "IEEE Standard Test Procedure for Polyphase Induction Motors and Generator," pp. 1–115, Feb. 2018.
- [44] Y. Xu and D. C. Aliprantis, "Wound-rotor induction machine model with saturation and high-frequency effects," in *Proc. Int. Elect. Mach. (ICEM) Conf.*, pp. 1838–1844, 2014.
- [45] S. D. Sudhoff, D. C. Aliprantis, B. T. Kuhn, and P. L. Chapman, "Experimental characterization procedure for use with an advanced induction machine model," *IEEE Trans. Energy Convers.*, vol. 18, no. 1, pp. 48–56, Mar. 2003.
- [46] S. Chiniforoosh et al., "Definitions and applications of dynamic average models for analysis of power systems," *IEEE Trans. Power Del.*, vol. 25, no. 4, pp. 2655–2669, Oct. 2010.
- [47] (MathWorks Inc.) *Simulink Software User Manual*, 2021, [Online]. Available: <https://www.mathworks.com>.
- [48] (OPAL-RT Technologies) *RT-LAB Quick Start Guide*, 2020, [Online]. Available: <https://www.opal-rt.com>.

- [49] N. Amiri, S. Ebrahimi, and J. Jatskevich, "Efficient simulation of wind generation systems using voltage-behind-reactance model of doubly-fed induction generators and average-value model of switching converters," in *Proc. IEEE First Ukraine Conf. Electrical and Computer Engineering (UKRCON)*, 2017, pp. 605–610.
- [50] S. C. Foroosh, L. Wang, and J. Jatskevich, "A simple induction machine model for predicting low frequency dynamics," in *Proc. Canadian Conf. Electrical and Computer Engineering*, 2008, pp. 1655–1660.
- [51] A. Narang, B. K. Gupta, E. P. Dick, and D. Sharma, "Measurement and analysis of surge distribution in motor stator windings," *IEEE Trans. Energy Convers.*, vol. 4, no. 1, pp. 126–134, Mar. 1989.

Appendices

Appendix A : Parameters for Case Study System of Section 2.2

Parameters of the induction motor [17]:

Three-phase Squirrel-cage IM, 460V, 50hp, 1705rpm, 4 poles, $r_s = 0.087 \Omega$, $X_{ls} = 0.302 \Omega$,
 $X_m = 13.08 \Omega$, $r_r = 0.228 \Omega$, $X_{lr} = 0.302 \Omega$, $J_{machine} = 1.662 \text{ kg.m}^2$, $T_b = 198 \text{ N.m}$, $f_b = 60 \text{ Hz}$.

Compressor torque-speed characteristics and inertia:

$$T_m = 0.2T_b + 0.8T_b \frac{P^2}{4\omega_b^2} \omega_{rm}^2, \quad J_{fan} = 0.5 \text{ kg.m}^2$$

Parameters of the line impedance:

$$r_{line} = 6.21 \text{ m}\Omega, \quad L_{line} = 32.53 \text{ }\mu\text{H}.$$

Parameters of the volts-per-hertz drive system:

$$\begin{aligned} \text{Sine Triangle PWM,} \quad V_{dc} &= 1051 \text{ V,} & m_f = f_{sw} / f_b &= 20, & f_{sw} &= 1.2 \text{ kHz,} \\ \tau_{reg.} &= 0.1029, & \text{SRL}_a(\alpha) &= \pm 60 \text{ rad/s,} & \beta &= \pm \omega_b / 40. \end{aligned}$$

Appendix B : Parameters for Case Study System of Section 3.2

Parameters of the three-phase squirrel-cage Y/Δ IM:

Rated power: 50 hp, rated voltage: 460 V, poles: 4,
speed: 1705 rpm, $J = 1.662 \text{ kg.m}^2$, $r_s = 0.261 \ \Omega$,
 $r_{r1} = 0.342 \ \Omega$, $r_{r2} = 0.684 \ \Omega$, $X_{ls} = 0.906 \ \Omega$,
 $X_{lr} = 0.906 \ \Omega$, $X_m = 39.24 \ \Omega$.

Parameters of the power grid:

$V_{line} = 460 \text{ V}$, $f = 60 \text{ Hz}$.

Parameters of the line impedance:

$R_{line} = 53.8 \text{ m}\Omega$, $L_{line} = 0.2813 \text{ mH}$.

Appendix C : Parameters for Case Study System of Section 4.2

Induction motor parameters for series–Y stator winding configuration:

Parameters	Value
Rated Power / Voltage / Poles	7.5hp / 460V / 4
Rated Current / Speed	9.5A / 1770rpm
Inertia / Frequency	0.0394kg.m ² / 60Hz
Low-Frequency Parameters	
r_s, r_r	1.0283Ω, 0.4422Ω
L_{ls}, L_{lr}, L_m (unsaturated)	9.1mH, 9.1mH, 143.8mH
High-Frequency Parameters [7]	
C_{g1}, C_{g2}	356.24pF, 1.3624nF
R_{g1}, R_{g2}	20.04Ω, 757.2Ω
L_{ls}, R_e	10.4mH, 3.2893kΩ
R_t, L_t	1368Ω, 5.6mH
C_t, L_c	171.86pF, 66μH
Bearing Circuit Parameters	
C_{ws}, C_{rw}	2.0435nF, 2.2007nF
$C_{sr}, C_{b,DE}, C_{b,NDE}$	28.202nF, 204pF, 204pF

Induction motor parameters for parallel-Y stator winding configuration:

Parameters	Value
Rated Power / Voltage / Poles	7.5hp / 230V / 4
Rated Current / Speed	19A / 1770rpm
Inertia / Frequency	0.0394kg.m ² / 60Hz
Low-Frequency Parameters	
r_s, r_r	0.2571Ω, 0.1106Ω
L_{ls}, L_{lr}, L_m (unsaturated)	2.3mH, 2.3mH, 36mH
High-Frequency Parameters [7]	
C_{g1}, C_{g2}	712.49pF, 1.3624nF
R_{g1}, R_{g2}	10.02Ω, 378.6Ω
L_{ls}, R_e	2.6mH, 822.3Ω
R_t, L_t	684Ω, 2.8mH
C_t, L_c	171.86pF, 33μH
Bearing Circuit Parameters	
C_{ws}, C_{rw}	2.0435nF, 2.2007nF
$C_{sr}, C_{b,DE}, C_{b,NDE}$	28.202nF, 204pF, 204pF

Calculations of CM and DM Voltages and Currents of Three-Phase IM-Drive System [27]:

The equations to calculate the CM and DM voltages and currents of a three-phase variable frequency drive system can be expressed as follows:

$$v_{CM} = \frac{1}{3}(v_{ag} + v_{bg} + v_{cg}), \quad i_{CM} = \frac{1}{3}(i_{as} + i_{bs} + i_{cs}), \quad (C.1)$$

$$v_{DM} = \frac{1}{3}(2v_{ag} - v_{bg} - v_{cg}), \quad i_{DM} = \frac{1}{3}(2i_{as} - i_{bs} - i_{cs}). \quad (C.2)$$